Title
Cryo-EM Studies of Microtubules and Bacterial Nanocompartments

Author
LaFrance, Benjamin

Publication Date
2020

Peer reviewed|Thesis/dissertation

Cryo-EM Studies of Microtubules and Bacterial Nanocompartments

By

Benjamin J LaFrance

A dissertation submitted in partial satisfaction of the

requirements for the degree of

Doctor of Philosophy

in

Molecular and Cell Biology

in the

Graduate Division

of the

University of California, Berkeley

Committee in charge:

Professor Eva Nogales, Chair
Professor David Drubin
Professor Karen Davies
Professor Seung-Wuk Lee

Summer 2020

Cryo-EM Studies of Microtubules and Bacterial Nanocompartments

By
Benjamin J LaFrance

Abstract

Cryo-EM Studies of Microtubules and Bacterial Nanocompartments

By

Benjamin J LaFrance

Doctor of Philosophy in Molecular and Cell Biology

University of California, Berkeley

Professor Eva Nogales, Chair

This dissertation focuses largely on structure-function relationship of microtubules, with a supplemental focus on bacterial nanocompartments known as encapsulins.

Microtubules (MTs) are an essential component of the eukaryotic cell. MTs are crucial for intracellular trafficking, cellular division, and motility, along with many other functions within the cell. The building blocks of a MT are tubulin heterodimers, which are GTPases that self-assemble to form a hollow, cylindrical MT architecture. The diversity of MT functions is achieved in part by a curious phenomenon known as dynamic instability whereby MTs are in a constant state of flux between growth and catastrophic depolymerization. These dynamics are directly linked to the nucleotide state of the MT, whereby the interplay the GTP and GDP nucleotide states determines the propensity for growth or shrinkage. The intrinsic regulation of dynamic instability, in addition to extrinsic regulation by various MT-associated proteins (MAPs), is absolutely critical for proper cellular function.

Cryo-electron microscopy (cryo-EM) was used to directly visualize these important biological assemblies in their native states. The first aspect of my work was to determine how the nucleotide state or the binding of common MAPs (EBs and Kinesins), affected the MT structure. Previous MT structures required MAP-binding to act as fiducials in order to facilitate high-resolution, and Chapter One of this dissertation shows the first high-resolution structures of undecorated MTs bound to various different nucleotides. The next aspect of my work was to examine the GTP-bound MT structure, in order to learn how certain MAPs specifically recognize the GTP state, and the conformational dynamics that occur upon GTP hydrolysis. Prior to this study, the MT field has used a GTP analog, GMPCPP, as a proxy for the GTP bound state. However, no one had actually observed MTs in the GTP state. Chapter Two in this dissertation uses mutated recombinant human tubulin that is hydrolysis-deficient to trap MTs that are truly GTP-bound. I found that these tubulin mutants are an invaluable platform for studying MTs. However, it appears that some mutants appear to create non-physiological assemblies, creating caveats for this system similar to the imperfections of nucleotide analogs.

The last chapter of this dissertation is the culmination of work using cryo-EM to better understand the assembly principles for a bacterial nanocompartment known as the encapsulin. Encapsulins were first discovered in 2008, and are typically composed of an enzymatic cargo confined within a proteinaceous shell. This compartmentalization can provide the cell with protection from toxic intermediates, or help with increasing local concentration to make the reaction more efficient. The methods driving cargo encapsulation to support these diverse functions remained unknown. For one encapsulin species, I determined how the cargo enzyme was associated with the encapsulin shell, and found that encapsulin cargos do indeed use a form of symmetry-matching. In this experiment, I found that a pentameric cargo protein binds at the pentameric vertices of the encapsulin shell, thus regulating where the cargo is within the compartment as well as the stoichiometry of cargo encapsulation. Serendipitously, while purifying this encapsulin, I also realized it was a previously overlooked flavoprotein. Given the fact that the cargo enzyme is a ferritin-like protein performing redox chemistry, this flavoprotein designation is very intriguing and warrants additional experiments.

Taken together this dissertation utilizes cryo-EM as a tool to probe the structural underpinnings that drive microtubule and encapsulin assembly and function.

Preface

It seems fitting to begin a dissertation on electron microscopy with quotes from two scientists that revolutionized our ability to observe both the big and the small. Robert Hooke, an early developer of the first microscopes, in his unabashed hubris, exclaimed, “there is nothing so small as to escape our inquiry”. After seeing the progression of the cryo-EM field throughout my graduate training, I’m inclined to agree with Hooke. My goal in going to graduate school was to gain significant technical training in cryo-EM, in order to better understand the relationship amongst the proteinaceous building blocks of cells. Any successes toward this goal are much more relevant to another quote from Hooke’s rival—Isaac Newton—who spoke with much more humility in saying, “If I have seen further, it is by standing on the shoulders of Giants.” That is most certainly the case, as you will see in the acknowledgements.

The body of research presented within in this dissertation occurred entirely in the last two years of my graduate work, with the first four years working on a project that was simultaneously being pursued by another group which was ultimately quicker to publish. The chapters discussed within this dissertation explore the structure/function relationships for two different biological systems—microtubules and bacterial nanocompartments—through the lens of an electron microscope. If any of those topics blow your hair back, please feel free to peruse my modest ‘*Waste Book*’ in the pages that follow (stealing another term from Newton).

Acknowledgements

The work described in this dissertation would not have been possible without the support of a few of my giants. I would first like to thank Eva for providing me the framework to pursue my research interests in her lab. It felt like limitless funding and free reign, which was the perfect environment to develop skills as an independent scientist. I would also like to immediately thank my committee members (David Drubin, Karen Davies, and Seung-Wuk Lee) who have been supportive, accommodating, and helpful for the past 6 years.

Thank you to all the lab mates who made it a joy to come to work every day. First and foremost, Basil—your unyielding generosity in thoughtfully answering every question I've ever asked without a single complaint is unparalleled. You will be a legendary PI. Avi—your late-night discussions while I work through a problem are invaluable. Never have I seen anyone as dedicated to science as you. Simon— your infectious sense of humor and infinite German dichos will stay with me forever. My next job is in ecology studying the larvae resulting from lusty newts… oh, what a profound impact you've had. Sarah—from delicious cakes to being the best lab citizen, your generosity is unequaled. Thank you. Kelly—you are my science role model and an absolute rock star while staying so down-to-earth. I don't know how you do it. Last, but not least, Stuart—your patience, expertise, sincerity, and mentoring made me feel at home in the microscope room. I think of you and the 5-item checklist every single time I close the column valves.

Thank you to the 'Lifers', Patricia, Jie, Teresa, and Abhiram. The microscopes wouldn't run, our storage tanks would be dry, the computers would be paperweights, and there would be no lab equipment to work with. I never would have finished my PhD without you. Teresa—without a hint of CRISPRing, you have been more of a mentor than you will ever know… both in how I approach science and my life.

I would also like to thank all my collaborators, and specifically Rob and Dave. What a great throw back to work on virus-like particles with you and characterize a new encapsulin.

On the topic of VLPs, I'd like to thank Trevor Douglas. I'd still be washing dishes at Miller Dining Hall if it weren't for you. Instead, science and art are integral to my everyday life, and will be forever. Thank you for teaching me a new way to see the world. You are a fantastic neighbor, mentor, and friend. Masaki, all of my knowledge as a bench scientist is thanks to your training. I'm so excited you get to mentor many more young scientists at Fresno State.

Katie—I've always said Berkeley is just a basecamp. Over the years, I'm realizing home is with you. Thanks for letting me use your shower while I live out of a van.
Ma and Pa— Thanks from your favorite son. I couldn't hit the broadside of a barn if I was born in it without your love and support over the years.

Table of Contents

List of Figures

Chapter One

Separating the Effects of Nucleotide and EB Binding on Microtubule Structure

Note: Prior to this study, all high-resolution cryo-EM microtubule structures were determined in complex with a microtubule associated protein (often EB3 or kinesin). These associated proteins act as a fiducial to differentiate the highly similar alpha and beta tubulin subunits. Upon binding to microtubules, these proteins likely effect the microtubule structure, and consequently hindered our ability to understand the true nature of an undecorated microtubule. The work herein describes the protocols and experimental set-ups designed to determine the structure of undecorated microtubules. These results act as a baseline for future studies regarding how associated proteins interact with microtubules, as well as aid in our fundamental understanding of how microtubules behave. Much of this work was made possible by significant technical advances from Rui Zhang [1], a post-doctoral researcher in the Nogales Lab, and together we used these advances to facilitate this study.*

1.1 Abstract

Microtubules (MTs) are polymers assembled from αβ-tubulin heterodimers that display the hallmark behavior of dynamic instability. MT dynamics are driven by GTP hydrolysis within the MT lattice, and are highly regulated by a number of MT associated proteins (MAPs). How MAPs affect MTs is still not fully understood, partly due to a lack of high-resolution structural data on undecorated MTs, which need to serve as a baseline for further comparisons. Here we report three structures of MTs in different nucleotide states (GMPCPP, GDP and GTPγS) at near-atomic resolution and in the absence of any binding proteins. These structures allowed us to differentiate the effects of nucleotide state versus MAP binding on MT structure. Kinesin binding has a small effect on the extended, GMPCPP-bound lattice, but hardly affects the compacted GDP-MT lattice, while binding of EB proteins can induce lattice compaction (together with lattice twist) in MTs that were initially in an extended and more stable state. We propose a MT lattice-centric model in which the MT lattice serves as a platform that integrates internal tubulin signals such as nucleotide state, with outside signals such as binding of MAPs or mechanical forces, resulting in global lattice rearrangements that in turn affect the affinity of other MT partners and result in the exquisite regulation of MT dynamics.

* Part of the work presented in this chapter has been published previously in the following manuscript:
Rui Zhang, Benjamin LaFrance, Eva Nogales. *Separating the Effects of Nucleotide and EB Binding on Microtubule Structure.* PNAS, 2018.

1.2 Introduction

Microtubules (MTs) are hollow tubes composed of αβ-tubulin heterodimers that stack head-to-tail to form linear protofilaments (PFs), which in turn associate laterally to define a cylindrical wall. In most eukaryotic cells, 13-PF MTs are the dominant form [2, 3], although MTs with different PF numbers have been reported for certain species [4]. The prevalence for 13-PFs *in vivo* could be due to the fact that MTs are typically nucleated from γ-tubulin ring complex (γ-TuRC) [5-7], which has been proposed as a template for 13-PF MT, and/or because MTs assemble in the presence of MT associated proteins (MAPs), such as end-binding proteins (EBs) and doublecortin, that bind across PFs and strongly promote the formation of 13-PF MTs, as observed *in vitro* [8-11]. Budding yeast MTs assemble predominantly as 12-PFs *in vitro*, but also shift towards 13-PFs in the presence of either Bim1 (yeast homolog of EB) or mammalian EBs [12, 13]. It has also been proposed that tubulin isoforms and posttranslational modifications of tubulin are important determinants of MT geometry [4]. However, it is unclear whether these factors directly influence MT structure or whether they do so indirectly, by defining the set of MAPs that interact with the MT.

Most MTs, whether assembled *in vitro* or *in vivo,* have a "seam" [14-17], where the lateral interactions between PFs are heterotypic (α-tubulin interacts with β-tubulin), whereas the rest of the MT has homotypic lateral interactions (α-α or β-β contacts). It is unclear what the physiological relevance of the seam is, although roles in MT growth and shrinkage have been proposed [14]. The MT seam has also been suggested to provide a unique binding site for MAPs [9, 14, 18], although no seam-binding protein has been identified yet. More recently, other biological systems that also possess a seam have been reported, such as a "mini microtubule" [19] and a flagellar filament [20] found in bacteria.

αβ-tubulin forms a stable heterodimer following its biogenesis, with each subunit bound to a guanine nucleotide [21, 22]. The GTP bound at the N-site (non-exchangeable site on α-tubulin) is always buried at the α-β interface within the dimer, is never hydrolyzed, and plays a purely structural role [23]. The GTP bound to the E-site (exchangeable site on β-tubulin), on the other hand, can be exchanged in unpolymerized tubulin dimers and is hydrolyzed to GDP within the MT following dimer addition to the lattice [24]. This hydrolysis results in MTs that are highly dynamic and undergo stochastic switches between growth and shrinkage phases, the hallmark phenomenon known as dynamic instability [25]. MTs will continue to grow as long as there is a cap of GTP-bound tubulin at their ends [26, 27], but loosing this GTP-cap makes the MT unstable and prone to depolymerization. Highlighting the importance of MT dynamics, the leading anticancer drug Taxol inhibits cell division by stabilizing MTs and suppressing their dynamic properties [28-30].

Recently, high-resolution cryo-electron microscopy (cryo-EM) allowed us to directly visualize MTs in different nucleotide states with unprecedented detail [31, 32]. Comparison of MTs bound to GDP and the slowly-hydrolyzable GTP analog GMPCPP (which mimics the GTP state at growing MT ends; see Discussion) revealed a ~2 Å lattice

compaction occurring at the interface between tubulin dimers that is mainly due to conformational changes in α-tubulin. We proposed that this lattice compaction generates strain inside the MT lattice that will ultimately be released upon MT depolymerization [31, 32]. It is worth noting that these cryo-EM studies used bound kinesin motor as a fiducial marker on the MT in order to distinguish between the highly similar α-and β-tubulin structures during image analysis. This fact left open the possibility that kinesin itself could influence MT structure, complicating the interpretation of the observed effects attributed to GTP hydrolysis.

MT dynamics are highly regulated by a number of MAPs. Among them is a family of proteins named plus-end tracking proteins (+TIPs), which selectively accumulate at the growing ends of MTs [33]. The EB proteins mentioned above are the central hub of the +TIPs network, and many other +TIPs hitchhike on EBs in order to track with the MT plus ends [34]. Recent studies showed that EBs influence MT dynamics by promoting MT growth, but also by increasing the frequency of catastrophes, the switch from MT growth to shrinkage [11, 35]. *In vitro*, EB proteins bind with high affinity to GTPγS-MTs [11, 36], suggesting that GTPγS-MTs may mimic some unique structural feature at the growing end of MTs. Recently, we reported the high-resolution structure of EB3-decorated GTPγS-MT showing a compacted MT lattice with a twist that is different from either the GMPCPP- or GDP-MT state [31]. However, it was unclear whether this unique MT lattice was a result of the nucleotide state (GTPγS) or the EB binding. We also showed that through copolymerization with GMPCPP-bound tubulin, EB3 promoted both the rapid hydrolysis of this slowly-hydrolyzable GTP analog within the MT lattice, and the accompanying lattice compaction [31]. A similar effect was observed for the budding yeast EB3 homolog, Bim1, which also induced lattice compaction for the otherwise extended dynamic budding yeast MTs [12, 13].

Here we report three high-resolution structures of MTs in different nucleotide states, GMPCPP, GDP and GTPγS, in the absence of any binding proteins. These structures of undecorated MTs posed technical challenges that we have only recently been able to overcome [1], allowing us to separate the effects of nucleotide and MAP binding on MT structure. We also demonstrate that, at high concentrations, EBs can bind and induce partial lattice compaction of a preformed 14-PF GMPCPP-MT, a MT lattice type that is far from EBs' ideal binding platform, further supporting our previous model that EB binding alters the MT lattice [31].

1.3 Results and Discussion

1.3.1 Structures of undecorated GMPCPP- and GDP-MTs

We recently developed a cryo-EM data processing protocol that is able to rely on small structural differences between α- and β-tubulin to determine the correct αβ-tubulin register and seam location in MT images. The protocol considers all possible MT-symmetry related solutions during image alignment, then selects the best match to the experimental image [1]. This protocol overcomes the need of a tubulin dimer marker, such as a kinesin or EB [11, 16, 17, 31, 32], and works well even for undecorated MTs. The

success of the protocol is demonstrated by the clear distinction between α and β tubulin densities in the resulting cryo-EM reconstructions (Figure 1.1A). For example, the S9-S10 loop, which is longer in α-tubulin, is clearly resolved and easily distinguished between α- and β-tubulin (Figure 1.1C). It is also reflected by the correct seam configuration displayed in the asymmetric (C1) reconstruction, that is, without application of pseudo-helical symmetry (Figure 1.1D). Using this data processing protocol, we have now determined the structures of undecorated GMPCPP- and GDP- MTs at atomic resolution (Supplemental Table 1.1). In both datasets, 14-PF MTs were the dominant form (Figure 1.1B).

For further quantitative analysis of the MT structure, we considered two helical parameters, the “dimer rise” and the “dimer twist”, in order to describe the MT lattice in different conditions. The dimer rise and dimer twist are defined as a set of translational and rotational operations that relates one tubulin dimer (i.e. one MT asymmetric unit) to the adjacent tubulin dimer within the same PF (Figure 1.2A). In other words, they are helical parameters for the 14-start (or 13-start, for a 13-PF MT) helix of the MT (Figure 1.1A). Another set of parameters we find useful in describing a certain MT lattice are the intra- and inter-dimer distances (Figure 1.2B). The intra-dimer distance is defined as the distance between two tubulin subunits sandwiching the non-hydrolyzable GTP at the N-site, while the inter-dimer distance is that between two tubulin subunits sandwiching the exchangeable nucleotide at the E-site.

Upon comparing undecorated MTs with our previously reported kinesin-decorated MTs [31, 32] (Figure 1.2C-D, Supplemental Table 1.1), we find that kinesin-1 binding shortens the spacing between longitudinally interacting tubulin dimers (the dimer rise) of the GMPCPP-MT by 0.7 Å. Interestingly, the spindle assembly factor TPX2 has the opposite effect on the GMPCPP-MT, slightly increasing the dimer rise by 0.3 Å [37]. On the other hand, kinesin-1 binding hardly affects the lattice spacing of the already compacted GDP-MT. Similarly, kinesin-1 binding has a small shortening effect on the dimer rise of EB3-decorated GDP-MT (0.1 Å) or EB3-decorated GTPγS-MT (0.4 Å), with the caveat that EB3 binding is reduced in the presence of the kinesin due to a small overlap of the two binding sites on the MT surface [31]. The dimer rise of the undecorated GDP-MT is also very similar to that of the EB3-decorated GDP-MT, suggesting that GDP-MT may represent the most compacted state of the MT, likely correspond the tubulin conformation storing the largest amount of strain within the lattice [31, 38]. It should be noted that among all the MT states we visualized, the intra-dimer distance remained relatively unchanged, presumably due to the constant presence of GTP at the N-site (Figure 1.2B and Supplemental Table 1.1).

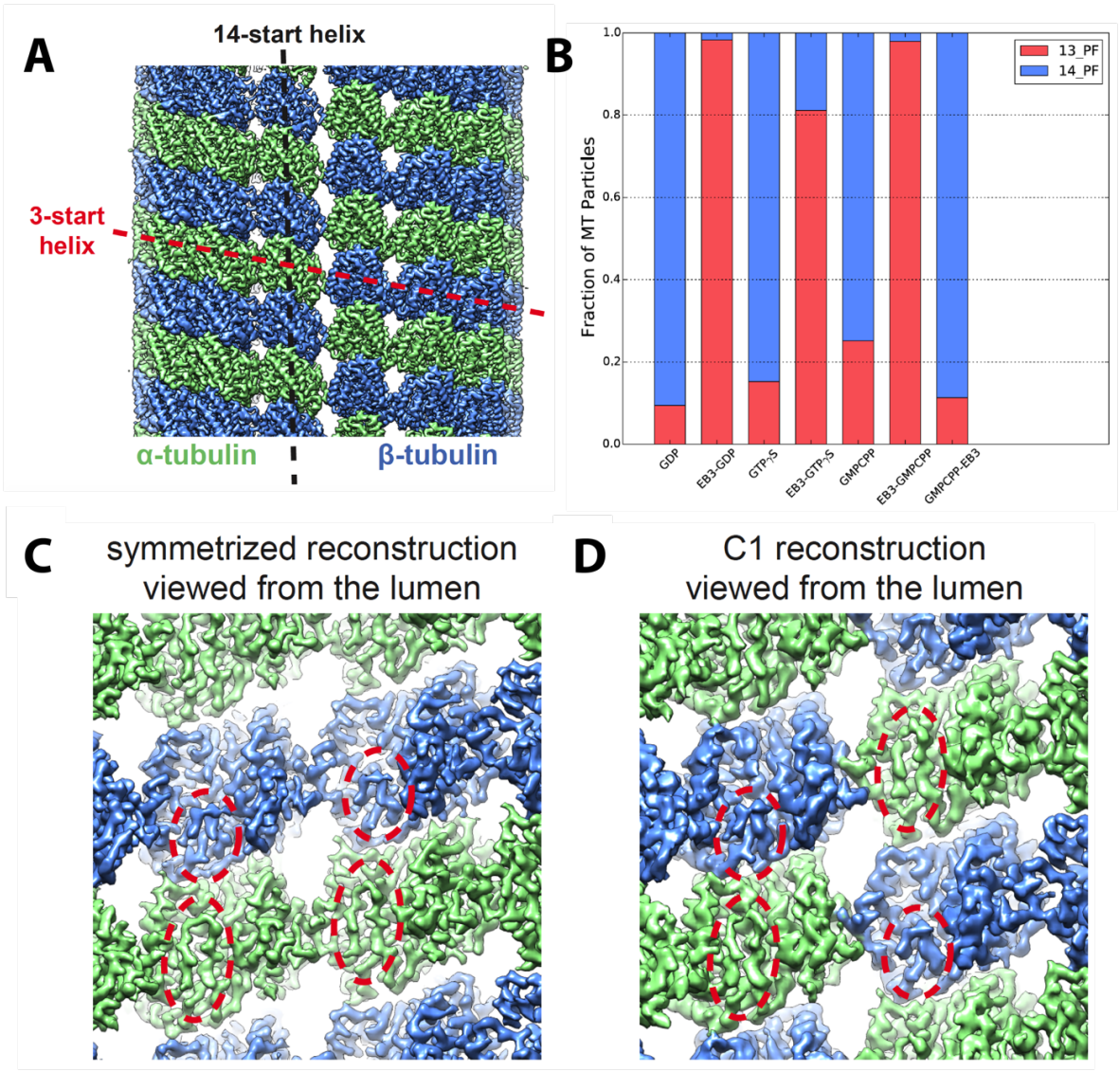

Figure 1.1: High-resolution structure of undecorated MTs. (A) Surface rendering of a cryo-EM density map of undecorated GMPCPP-MT with pseudo-helical symmetry applied. α and β tubulin are colored in green and blue, respectively, throughout the manuscript, unless specified. The red and black dash lines denote the 3-start and 14-start (or 13-start, in the case of 13-PF MT) helices of the MT, respectively. **(B)** Histogram of the PF distribution for MTs in different states. **(C)** Zoomed-in view of the cryo-EM reconstruction in (A), viewed from the lumen. The red dashed circles highlight the density region corresponding to the S9-S10 loop, which has different lengths in α and β tubulin. **(D)** Zoomed-in view (from the lumen) of the corresponding C1 reconstruction of undecorated GMPCPP-MT without applied pseudo-helical symmetry, showing the configuration at the seam.

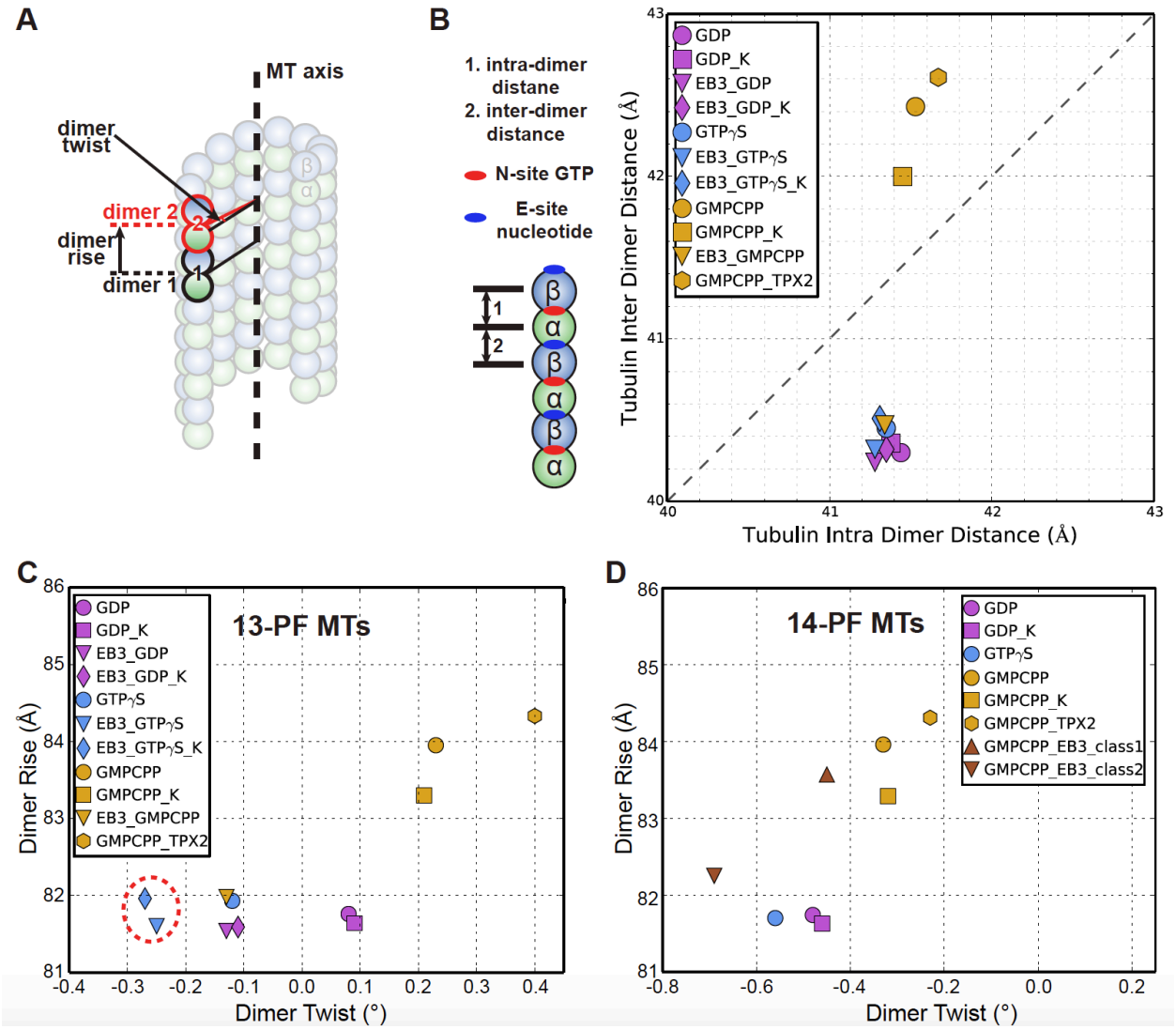

Figure 1.2: Variation of lattice parameters for different MT states (A) The MT dimer rise and dimer twist are defined as the translational and rotational operations that relate one tubulin dimer (dimer 1, outlined in black) to the adjacent tubulin dimer (dimer 2, outlined in red) along the same PF. The dimer rise and twist are measured directly from the C1 reconstruction of each MT state (see Supplemental Table 1.1). **(B)** Plot of inter-dimer vs intra-dimer distances for each MT state. Here the inter-dimer distance is defined as the distance between two tubulin subunits sandwiching the exchangeable nucleotide at the E-site, while the intra-dimer distance is the distance between two tubulin subunits sandwiching the non-hydrolyzable GTP. The values of the inter-dimer and intra-dimer distances were calculated from the atomic models of each state, using the mean of the Cα distances between α- and β-tubulin for each pair of corresponding residues. **(C)** Plot of dimer rise versus dimer twist for 13-PF MTs in different states. The red dashed circle indicates the values corresponding to the optimal MT lattice for EB3 binding. **(D)** Plot of dimer rise versus dimer twist for 14-PF MTs in different states. In the figure legend, if the name of the binding protein comes before the nucleotide (e.g., EB3-GMPCPP), then the MTs were polymerized in the presence of the binding protein. If the name of the binding protein comes after the nucleotide (e.g., GMPCPP-EB3), then the protein was added to preformed MTs. 'K' denotes kinesin. This nomenclature is used consistently throughout the manuscript.

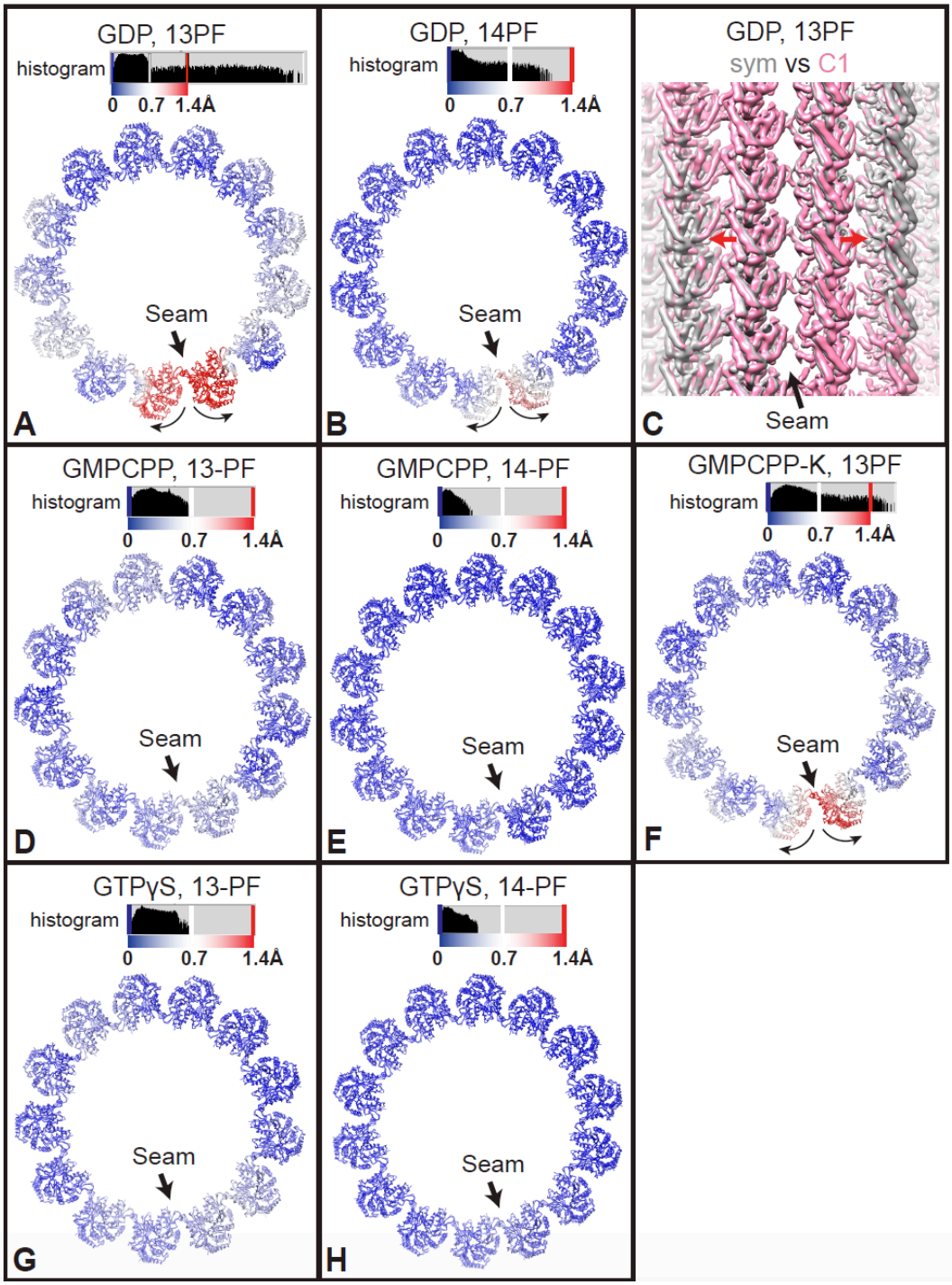

Figure 1.3: Lateral contacts at the MT seam for MTs with different stabilities. The panels show comparisons of the C1 and the symmetrized reconstructions of different MT states. **(A-B, D-G)** Cα-atoms displacements between atomic models of one helical turn of tubulin dimers for the C1 and the symmetrized reconstructions of different MT states, with deviations colored from blue to red. The histograms of Cα-atoms displacements are also shown above the atomic models. **(C)** Superimposition of the C1 and the symmetrized reconstructions of 13-PF GDP MT, showing the seam opening in the C1 reconstruction (red arrows). Both reconstructions have been low-pass filtered to 7Å resolution for easier comparison.

As shown in one of our previous studies, a straightforward method to detect a deviation from a true cylindrical arrangement in the MT is to superimpose the atomic models fitted into the C1 and into the symmetrized reconstructions [31]. Following this procedure, we found that in the 13-PF GDP-MT, the two PFs across the seam are significantly further apart from each other than the PFs in the rest of the MT (Figure 1.3A). This deformation at the seam is also the case for the 14-PF GDP-MT, but to a lesser extent (Figure 1.3B). The seam opening for 13-PF GDP-MTs is also apparent by directly superimposing the densities of the C1 and symmetrized reconstructions (Figure 1.3C). In both the 13-PF and 14-PF GMPCPP-MTs, the position of the two PFs across the seam is almost identical for the C1 and the symmetrized reconstructions (Figure 1.3D-E). Previously, we reported a slight seam opening for the 13-PF kinesin-decorated GMPCPP-MTs (Figure 1.3F) [31]. We can now attribute this difference to kinesin-1 binding, which changes the lattice spacing of GMPCPP-MT (Figure 1.2C-D, Supplemental Table 1.1), therefore altering the lateral interactions between PFs at the seam.

1.3.2 Structures of undecorated GTPγS-MT

In previous work, we obtained the high-resolution structure of EB3-decorated GTPγS-MTs, which was polymerized from GMPCPP-MT seeds through coassembly with EB3 [31]. However, at that time we were not able to assemble GTPγS-MTs in the absence of EB3. Recently, we improved the experimental protocol, by significantly reducing the concentration of Mg^{2+} in the buffer and increasing the starting tubulin concentration and the polymerization time. With these modifications, we obtained a considerable amount of GTPγS-MT extensions out of the GMPCPP-MT seeds without needing to co-polymerize with EBs. Consistent with previous reports [36, 39, 40], no MT growth was observed in the absence of GMPCPP-MT seeds, supporting the idea that GTPγS-tubulin is a poor MT nucleator.

In the absence of EB proteins, the GTPγS-MT extensions follow the geometry (i.e. the PF number) of the GMPCPP-MT seeds, which are predominantly 14-PF (~80%) (Figure 1.1B). This is in stark contrast to the GTPγS-MTs copolymerized with high concentrations of EB3 (also requiring the seeds), which strongly promotes 13-PF MTs [31] (Figure 1.1D). After sorting out 13- and 14-PF MTs, we used two different image classification strategies in order to further separate the GMPCPP-MT seeds from the GTPγS-MT extensions. First, we classified the MT segments by measuring their lattice spacing using their layer lines in Fourier space (see Experimental Procedures). This layer-line analysis showed a bimodal distribution, with one mode corresponding to the peak observed for pure undecorated GMPCPP-MTs and the other mode corresponding to GDP-MTs (Figure 1.4A). A local average of seven adjacent segments, which significantly increases the signal-to-noise ratio [1], was used for this measurement. In addition, we also performed multi-reference sorting using two models with different MT lattice types (an extended GMPCPP-MT and a compacted GDP-MT) from our previous studies [31]. These two methods gave very consistent classification results, producing two major classes for both 13- and 14-PF MTs. One of the classes (class 1, which contains about 25% of the total particles) had exactly the same lattice parameters as we see for the undecorated

GMPCPP-MT (Figure 1.4B), and therefore should correspond to the GMPCPP-MT seeds. Class 2, which contains 75% of the total particles, had a compacted lattice (Figure 1.4B), very similar to the previously reported EB3-decorated GTPγS-MT, but with a lesser amount of lattice twist (as measured by dimer twist) (Figure 1.2D). This class should therefore correspond to the GTPγS-MT extensions. Typically, all the particles from the same MT are classified into the same class. Although the field of view that we used for high-resolution imaging is relatively small, we did occasionally capture transitions between GMPCPP-MT seeds and GTPγS-MT extensions. As a control, we also applied the same multi-reference sorting protocols to the pure undecorated GMPCPP-MT and GDP-MT datasets, and in each case, we obtained only one major class containing over 98% of the particles.

With regards to the lateral interactions between PFs across the seam, the C1 and symmetrized reconstructions for the undecorated GTPγS-MT were markedly similar for both 13-PFs and 14-PFs (Figure 1.3G-H). This result parallels our observations for GMPCPP-MTs (Figure 1.3D-E). In contrast, the two PFs across the seam are further apart from each other in the GDP-MT, especially in the case of the 13-PF GDP-MT (Figure 1.3A-C). The difference in lateral interactions at the seam may therefore relate to the stability of MTs bound to these non-hydrolyzable GTP analogs which are addressed later on.

1.3.3 EB3 induces lattice compaction of preformed 14-PF GMPCPP-MTs

Previously, we have shown that when copolymerizing EB3 with GMPCPP-tubulin, EB3 strongly promotes 13-PF MTs (Figure 1.1B), induces lattice compaction (Figure 1.2C), and stimulates the hydrolysis of the usually slowly-hydrolyzable GMPCPP [31]. To further understand the effects of EB3 on the MT lattice, we challenged EB3 with a MT type that is distinct from its favored MT substrate [31]. We first applied undecorated GMPCPP-MTs (predominantly 14-PF MTs and with an extended lattice) to the EM grid, and then washed the grid twice with highly concentrated EB3 before blotting and freezing. Under these experimental conditions, while EB3 did not change the PF number distribution of the pre-made 14-PF GMPCPP-MTs, it was able to bind and induce measurable changes in the lattice in terms of both lattice compaction and lattice twist. Although the plot of lattice spacing for all the MT segments does not show a bimodal distribution for the EB3-MT co-assembly (Figure 1.4C), using two distinct 3D references (corresponding to an extended GMPCPP-MT and a compacted GDP-MT), we separated the MT segments into two main classes (class 1 and class 2, which contains 30% and 70% of the total number of particles, respectively). Class 1 had an extended MT lattice that is very similar to the undecorated GMPCPP-MT (Figure 1.2D, 1.4D), and had weak density corresponding to EB3 (Figure 1.4E). In contrast, class 2 had a partially compacted lattice (Figure 1.2D, 1.4D), as well as stronger EB density (Figure 1.4F). Interestingly, both classes had a significantly more left-handed MT-lattice than the undecorated GMPCPP-MT (Figure 1.2D). Unfortunately, the limited resolution due to sample heterogeneity did not allow us to visualize if the GMPCPP at the E-site of the partially compacted class 2 had been hydrolyzed.

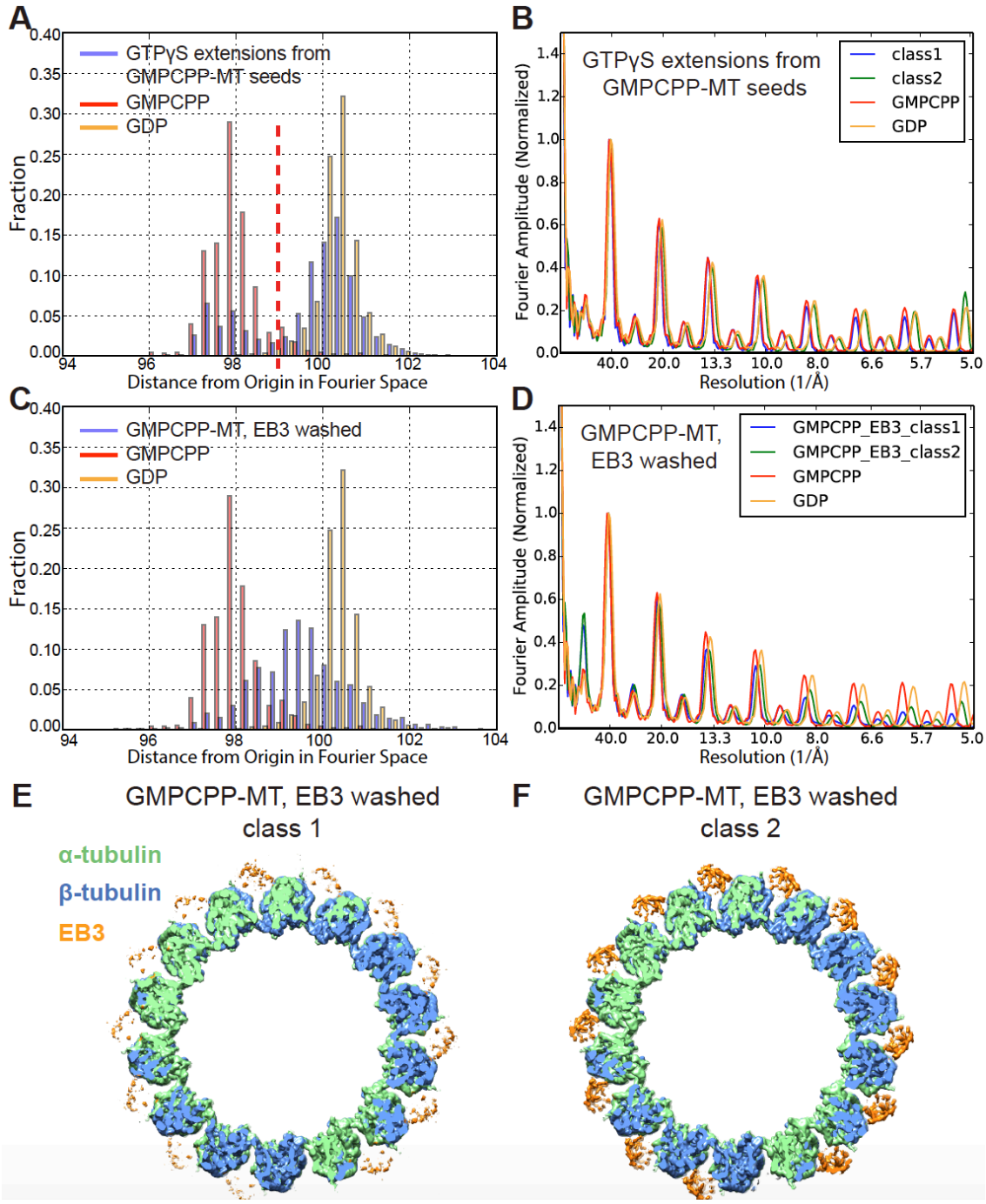

Figure 1.4: Separation of different MT lattice types for samples with a mixed population. **(A)** Histogram of layer line positions for each MT segment in the dataset of GTPγS growing from GMPCPP-MT seeds, showing a bimodal distribution (only 14-PF MTs are plotted in blue). The x-axis Fourier space unit is arbitrary. The red dashed line indicates the cutoff value we used to separate this dataset into two classes. The histograms of layer line positions for each MT segment in the datasets of the pure undecorated 14-PF GMPCPP-MT (red) and 14-PF GDP-MT (orange) are also shown for comparison (same for (C)). **(B)** Plot of layer line profiles for the reconstructions of the two classes observed in the dataset shown in (A). The layer line profiles of undecorated GMPCPP- and GDP-MT reconstructions are also shown for comparison (same for (D)). **(C)** Histogram of layer line positions for each MT segment in the dataset of EB3 washed GMPCPP-MTs (only 14-PF MTs are plotted in blue). **(D)** Plot of layer line profiles for the reconstructions of two classes present in the dataset of EB3 washed GMPCPP-MTs (14-PF). **(E, F)** Top view of the 3D reconstructions of class 1 and class 2, respectively. α-tubulin, β-tubulin and EB3 densities are shown in green, blue and orange, respectively.

These results indicate that a few EB3 molecules can affect MT lattice twist, but only a larger number of bound EB proteins can cause compaction and hydrolysis. The fact that particles from the same MT typically go to the same class after sorting suggests a cooperative effect once a certain number of EB proteins bind, likely mediated by a lattice switch into a conformation (the compacted state) that further facilitates EB binding. This model is consistent with the observation that higher concentration of EBs reduced the maturation time of MTs before a catastrophe [35].

1.3.4 GTP analogs and what they represent for MT structure and dynamics

As in the biochemical study of any GTPase, the study of tubulin has involved the use of non-hydrolyzable GTP analogs to dissect its function. GTPγS proved to have strange properties on tubulin assembly, somehow behaving more like GDP than GTP concerning its incapacity to nucleate MT formation [36, 39, 40]. The synthesis and use of GMPCPP, a slowly-hydrolyzable analog with reasonable affinity for the tubulin E-site that can promote MT assembly, showed it to be a much better mimic of GTP in its effect on tubulin self-assembly [41]. The near-atomic resolution structures of undecorated MTs discussed herein provide insights into how the two GTP analogs, GMPCPP and GTPγS, can have dramatically different effects on MT structure. The GMPCPP-bound MT has an extended lattice, while GTPγS-bound MT has a compacted lattice, even in the absence of EB protein. Thus, the GTPγS state of MTs appears more similar to the GDP than the GTP state, a structural result that parallels what is seen in some functional studies with this analog. Because GDP and GTPγS are, nevertheless, not identical in their effect on the MT as observed functionally and structurally (see below), we have proposed that GTPγS mimics a transition state in the nucleotide hydrolysis cycle, probably a GDP-Pi state [31]. Consistent with this proposal, high-resolution fluorescence microscopy has recently shown that EB1, which favors GTPγS-MTs as its substrate, binds to a region at the MT growing end that lags several tens of nanometers behind XMAP215 [35], which binds to the extreme end of MT, where the tubulin is presumably in the GTP state.

With regards to the state of GMPCPP-MTs, we have at least three major reasons that lead us to believe that the GMPCPP-MT is a good mimic of a true GTP state, as originally proposed [41]. First, both GTP-tubulin and GMPCPP-tubulin are relatively good nucleators, while tubulin in other nucleotide states (GDP and GTPγS) are not. Second, the GMPCPP-MT has a longitudinal inter-dimer distance, which depends on the nucleotide state at the E-site, that is closer to the mostly invariable intra-dimer distance (reflecting the constant GTP at the N-site), than that of the GDP- or GTPγS-MTs (Figure 1.2B, Supplemental Table 1.1). Finally, TPX2, a spindle assembly factor that is known to strongly promote MT nucleation [42, 43], probably by stabilizing early nucleation intermediates, shows strong binding specificity for both GMPCPP-MT seeds and the growing ends of MTs *in vitro* [43]. These observations suggest that there are common structural features among GMPCPP-MTs, the MT growing ends, and early nucleation intermediates, with the latter two presumably existing in a GTP state.

1.3.5 Effect of GTP hydrolysis on MT structure: strain and the seam

Our structural studies comparing MTs in the GMPCPP and GDP states have shown a ~2 Å lattice compaction upon GTP hydrolysis, which occurs at the polymerization interface between two tubulin dimers [31, 32]. This apparent lattice compaction is due to an internal domain rearrangement of every α-tubulin consisting of a relative rotation of the intermediate domain and the C-terminal helices of α-tubulin with respect to its N-terminal domain. Interestingly, this rotation from the GMPCPP to the GDP state is in the opposite direction from that observed in the proposed ‘‘ground state’’ represented by the crystal structures of unpolymerized tubulin [38, 44], suggesting that GTP hydrolysis generates mechanical strain that is stored in the MT lattice.

In addition to its effect on lattice compaction (as measured by dimer rise) just described, GTP hydrolysis has other structural consequences that are likely to be relevant for our understanding of MT dynamic instability. These include changes in lattice twist (as measured by dimer twist) and in the lateral contacts at the seam.

When comparing MTs in the same nucleotide state but with different PF numbers (e.g., 13-PF vs 14-PF), the structures are very similar at the PF level, although the PFs run with a different skew angle with respect to the MT axis (also referred to as “supertwist”, and mathematically related to the dimer twist). This skew angle generates the classical moiré pattern observed over long distances [45, 46] that is predicted by the “MT lattice accommodation model” proposed more than 25 years ago by Wade and colleagues [15]. On the other hand, comparison of MTs with the same PF number but in different nucleotide states (e.g., GTPγS vs GDP) shows that dimer twist changes slightly [31] (Figure 1.5A). This small shift between two longitudinally interacting tubulin dimers within the PF is likely due to the subtle rearrangement of hydrogen bonds at the E-site. Such a small shift accumulates over long distances, causing the PF to run at a slightly different skew angle (Figure 1.5A). Thus, both nucleotide state and PF number can alter the skew angle of PFs, which will inevitably change the structural details of the lateral contacts that hold the lattice together against strain, and therefore may affect the overall stability of the MT lattice.

The lateral interactions at the seam may be a direct read-out of the overall stability of the MT. We have observed that GDP-MTs are less “cylindrically” symmetric than the GMPCPP and GTPγS MTs (both of which are stable states). In GDP-MTs, the positions of the two PFs across the seam are further apart from each other than those observed for other PF pairs (Figure 1.3). It is likely that the α-β interaction at the seam is always intrinsically weaker than the homotypic (α-α or β-β) interactions at non-seam locations, regardless of the nucleotide state. Our studies indicate that when the MT lattice is placed under stress following GTP hydrolysis, this strain is first manifested in the “stretching” of the seam. Based on this observation, we propose that the seam would likely be the first place to crack open in a MT catastrophe event. Losing 1 of the ~13 lateral interactions that act as a whole to counteract the intrinsic curling tendency of individual PFs would then trigger the outward pealing of other PFs, as is often observed at the ends of

depolymerizing MTs [47]. Consistent with this idea, we have previously described how the MT stabilizing agent peloruside, which binds across both homotypic β-β interfaces and heterotypic α-β interfaces, also brings the two PFs across the seam closer to each other [48].

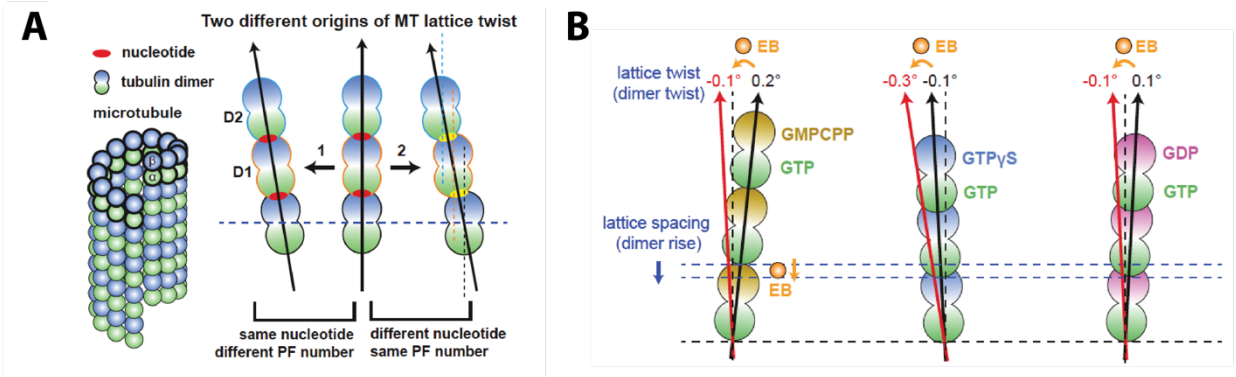

Figure 1.5: Cartoon diagram of the different origins of lattice twist and the effect of EB3 on MTs in different nucleotide states. **(A)** Relationships between nucleotide state, PF number and lattice twist (or PF skewing). (1) MTs with the same nucleotide but different PF numbers will naturally run at a different skew angle with respect to the MT vertical axis, but the tubulin structures are very similar at the PF level. (2) MTs with the same PF number but different nucleotides have a small amount of shift between two longitudinally interacting tubulin dimers along the PF. Such a small shift also accumulates over a long distance, causing the PF to run at a slightly different skew angle. **(B)** In each MT nucleotide state (GMPCPP, GTPγS and GDP), EB3 generates left-handed lattice twist (measured as dimer twist). EB3 also induces lattice compaction of GMPCPP-MT.

1.3.6 Effect of EB binding on MT structure and stability

In living cells, EBs track with growing MT ends, recognizing a structural state of the MT lattice that is dependent on its nucleotide content. Biophysical and structural studies indicate that EBs preferentially bind a state that is best mimicked *in vitro* by GTPγS-MT. In spite of the fact that both are compacted states, the GDP and GTPγS MT states are not identical. The 13-PF GTPγS-MT has a dimer twist (-0.1°) that is different from both the 13-PF GMPCPP-MT (0.2°) or the GDP-MT (0.1°) (Figure 1.2C, 1.5B, Supplemental Table 1.1). The unique dimer twist observed for GTPγS is likely to be recognized by EB proteins, which bind four tubulin dimers across two PFs and thus are particularly sensitive to PF skew.

By comparing the three nucleotide states (GMPCPP, GDP and GTPγS) of MTs with and without bound EB3, there is a clear trend that, at least at the high concentrations used in the cryo-EM studies, EB3 introduces additional left-handed lattice twist to whatever MT lattice it binds (even for 14-PF MTs). EB3 also induces lattice compaction, except when added to a lattice that is already fully compacted (Figure 1.2C-D, 1.5B). Very similar effects on MT lattice twist by the yeast homologs Bim1 and Mal3, have also been reported recently [12, 13, 49]. In the case of EB3, it appears that the MT conformation for maximal EB3 binding is a 13-PF MT with a compacted lattice (dimer rise of around 81.5 Å) as well as a relatively large left-handed lattice twist (dimer twist of around -0.3°) (Figure 1.2C, 1.5B, Supplemental Table 1.1). Our structural comparisons (Figure 1.5B) indicate that 13-PF GTPγS-MTs have the intrinsic capacity to fully accommodate this optimal EB binding site, and consequently have the highest affinity for EB3 [11, 36]. 13-PF GMPCPP-MTs and GDP-MTs, however, can only be partially modulated by EB3 towards its preferred

lattice conformation [31], even when EB3 is in excess, likely due to the suboptimal binding pocket for EB3, which spans four tubulin dimers across both longitudinal and lateral interfaces, in these alternative MT lattices.

Thus, the complex effect of EB proteins on MT dynamics is likely to be rooted in the duality of EB recognition of, and effect on, the MT lattice. As just mentioned, our structures show that EB binding leads to lattice compaction of the extended GTP state that is linked to GTP hydrolysis. So far, it is not possible for us to determine, from our structures alone, the causality of the process: does EB promote compaction that sterically facilitates hydrolysis, or is compaction a result of hydrolysis? Nevertheless, it is apparent that GTP hydrolysis ultimately results in a GDP state with a different lattice twist than that preferred by EB (i.e. that mimicked by GTPγS). Because each EB molecule binds across four tubulin dimers, EB is particularly sensitive to changes in lattice twist. We propose that the lattice twist in the GDP-MT correspond to a low affinity state for EB that causes it to come off the MT lattice, likely upon Pi release. The combination of effects on MT lattice that we see due to EB binding and nucleotide state provides a structural framework for a mechanistic understanding of the end-tracking behavior of EB proteins.

1.3.7 A lattice-centric model of MT dynamic instability and its regulation

A number of studies have shown that the structural state of the MT lattice can be modulated by different binding partners, especially when they are present in the high concentrations typically used for cryo-EM studies. The effects seen for these proteins further support a previously proposed model of structural plasticity for tubulin and MTs [50]. It appears that proteins that bind across the inter-dimer interface, such as EB proteins [11, 31], doublecortin [8, 51] or TPX2 [37], have stronger influence on MT lattice and MT dynamics than MT-binding proteins that bind within the tubulin dimer, such as dynein [52, 53], kinesin [16, 17], TTLL7 [54], PRC1 [55, 56] or WHAMM [57].

In addition to sensing the subtle lattice differences in straight MTs, it has been observed that several MAPs, such as TPX2 [43] or doublecortin [58, 59], can preferentially accumulate at curved regions of MTs, which can arise from deformations due to mechanical forces. Such curved MT regions may provide unique lattice configurations that are different from those in straight regions. For example, as recently proposed by Wittmann et al. [59], the convex or the concave side of the curvature may provide slightly larger or smaller dimer spacing, respectively, that can be preferentially recognized by MT binding partners.

It is believed that growing MT ends and early nucleation intermediates resemble open sheet structures [60-62]. Such lattice conformation, which will be absent in the MT shaft, can be recognized by certain MT binding proteins. In fact, consistent models have been proposed recently to explain the plus end recognition by EB proteins [63-65], the early nucleation intermediates recognition by TPX2 [37, 43], and also the minus end accumulation by CAMSAP [65].

We propose a MT lattice-centric model in which the MT lattice, either in straight or curved regions, serves as a platform in the cell to integrate multiple internal tubulin signals (i.e. nucleotide state, chemical modifications et al.) and outside signals (i.e. binding of MAPs, binding of stabilizing/destabilizing drugs or mechanical forces), and the resulting global lattice rearrangement in turn affects the affinity of its binding partners. In this way, the dynamics properties of MTs can be exquisitely regulated by the combinatorial and sometimes sequential binding of associated factors.

1.4 Material and Methods

1.4.1 Protein Purification

The human EB3 monomeric construct (residues 1-200) was expressed in BL21-CodonPlus-(DE3)-RIL cells and purified using His-tag affinity purification and size-exclusion, following a previously published protocol [31]. Porcine brain tubulin was purchased from Cytoskeleton Inc.

1.4.2 Cryo-EM Sample Preparation

The kinesin-decorated and undecorated GMPCPP-MT samples were prepared as previously described [31, 32]. We typically snap-freeze 5 µl aliquots of GMPCPP-loaded tubulin (that has been through one polymerization-depolymerization cycle) at 3 mg/ml for future use, e.g. to make GMPCPP-MT seeds. The undecorated GDP-MTs were made by polymerizing a 5 µl aliquot of 10mg/ml dynamic porcine MTs in CB1 buffer (80 mM PIPES pH 6.8, 1 mM EGTA, 1 mM $MgCl_2$, 1 mM GTP, 10% glycerol) for 45 min at 37°C. This was followed by a 20 min 16,000g centrifugation step at 37°C to pellet the 'assembly competent' MTs. The supernatant was discarded and the GDP-MT pellet was resuspended in 5 µl of warm CB1 buffer supplemented with 0.05% Nonident P-40, and repolymerized for 15-20 min prior to plunge freezing in liquid ethane.

GTPγS-MTs were obtained using the following procedure, which is adapted from a previously published protocol [36, 66]. First, we prepared GMPCPP-MT seeds from a frozen aliquot of GMPCPP-tubulin by incubation at 37 °C, stopping the polymerization by 10-fold dilution after just 2 mins in order to obtain relatively short MT seeds. The GMPCPP-MT seeds were pelleted and resuspended in equal volume of warm BRB80 buffer without GMPCPP. Next, Porcine tubulin powder (Cytoskeleton) was reconstituted to 10 mg/ml in CB1 buffer. After polymerizing MTs at 37 °C for 45 mins followed by centrifugation at 17,000 RCF for 15 min, MT pellets was resuspended in cold EM buffer with a lower Mg^{2+} concentration (80 mM PIPES, pH 6.8, 1 mM EGTA, 0.2 mM $MgCl_2$, 1 mM DTT, 0.05% Nonidet P-40) supplemented with 1 mM GTPγS (Roche), which causes MT depolymerization and tubulin E-site nucleotide exchange. After 20 mins, the GTPγS-loaded tubulin was diluted to 5 mg/ml concentration, and 15 µl of GTPγS-tubulin was warmed up to room temperature and mixed with 1 µl of pre-formed GMPCPP-MT seeds (~0.3 mg/ml). The sample was allowed to polymerize at 37 °C in EM buffer for about 45 mins before EM grid preparation.

To freeze the undecorated MTs, 3 µl of MT sample (diluted to ~0.2 mg/ml) was applied to a glow-discharged C-flat 1.2/1.3-4C holey carbon EM grid (Protochips). After 30 s

incubation time inside a Vitrobot (FEI) set at 25 °C for GMPCPP-MTs or 37 °C for GTPγS-MTs and dynamic MTs, the grid was blotted for 4 sec and plunged in liquid ethane.
For the experiment using preformed GMPCPP-MTs that were washed with EB3, we desalted EB3 into cold EM buffer using a Zeba Micro Spin desalting column (Thermo Scientific) and the sample was clarified by ultracentrifugation. 3 µl of the GMPCPP-MT sample was first absorbed to a glow-discharged EM grid. After 30 s incubation inside a Vitrobot set at 25 °C, the grid was washed twice with 3 µl of EB3 at 30 µM concentration (30 s incubation each time), before blotting and vitrification in liquid ethane.

1.4.3 Cryo-EM Data Collection

Three datasets (undecorated GMPCPP-MT, undecorated GDP-MT and kinesin decorated GMPCPP-MT) were collected using a 300 keV Titan Krios at the UCSF cryo-EM facility. A bigger dataset of undecorated GMPCPP-MT was collected using a 300 keV Titan Krios equipped with a Cs-corrector and a Gatan Image Filter (GIF) at the Center for Cellular Imaging (WUCCI) in Washington University in St. Louis (WUSTL). All other datasets were collected using a 300 keV low-base Titan microscope (FEI) located at UC Berkeley (UCB). All the data were collected using a K2 Summit direct electron detector (Gatan), in counting or super-resolution mode, with a dose rate of 8-9 electrons/pixel/s. All the samples were imaged under parallel illumination conditions, with a beam diameter of ~2 µm on the specimen. A defocus range from -0.5 to -2.5 µm was used. The data were collected using Leginon [67], SerialEM [68] and EPU (FEI) at UCB, UCSF and WUSTL, respectively. The data collection statistics are listed in Supplemental Table 1.1.

1.4.4 Image Processing

Drift correction for each movie stack was performed using the MotionCor2 program [69]. Then the contrast transfer function (CTF) parameters were estimated from the motion-corrected micrographs using Gctf [70]. In the next step, we manually selected MTs from the motion-corrected micrographs using the APPION image processing suite [71]. Then the selected MT images were computationally cut into overlapping boxes, with a ~80 Å non-overlapping region (along the MT axis) between adjacent boxes. The initial alignment parameters and PF number for each boxed MT segment were determined using multi-reference alignment (MRA) in EMAN1 [72]. MT segments with the same PF number were grouped and subjected to further structural refinement in FREALIGN v9 [73]. After that, we used a recently established data processing protocol to determine the αβ-tubulin register and seam location for each boxed MT segment [1]. The kinesin/EB3 decorated MTs and undecorated MTs were processed using exactly the same set of scripts, although in the case of undecorated MTs, a good reference model with clear distinction of α-, β-tubulin density was needed. Finally, 3D reconstructions (assuming either MT pseudo-helical symmetry or no symmetry) were performed using FREALIGN (sym=HP or sym=0). During the reconstruction process, particles are weighted based on their similarity scores with respect to the reference model, and 20% 'bad' particles with the lowest scores were discarded. For each MT state, the helical symmetry parameters (axial rise and azimuthal twist) corresponding to the 3-start helix or 13-start helix (i.e., dimer rise and dimer twist) of the MT were measured from the C1 reconstruction using the

relion_helix_toolbox program in RELION v2.1 [74], which gave results consistent with those we previously obtained [31] using the *hsearch_lorentz* program in the IHRSR package [75]. The final resolution for each reconstruction (Supplemental Table 1.1) was estimated by calculating the Fourier Shell Correlation (FSC) of one protofilament segment containing 3 adjacent tubulin dimers from the odd and even maps, using an FSC 0.143 criterion.

To separate the MTs based on their lattice spacing, we compute the MT 'super-particles' by averaging every 7 neighboring MT raw particles together using their alignment parameters obtained from FREALIGN [1]. This is based on the idea that due to the slow super-twist of MT, neighboring MT particles represent very similar view of the MT, even for the 14-PF MTs. In the super-particles, the signal-to-noise ratio (SNR) is greatly improved, therefore allowing us to precisely measure the spacing of layer lines in the 2D Fourier Transform of the image, which corresponds to the lattice spacing in real space. In the case of GTPγS MTs extended from GMPCPP-MT seeds, based on the shape of the histogram of the layer line spacing for all the super-particles, which displays a bimodal distribution, a cut-off value of 99 was determined to split the MT dataset into two homogenous subgroups (Figure 1.4A). In the case of preformed GMPCPP-MTs washed with EB3, it's hard to determine a cut-off value based on the histogram (Figure 1.4C), therefore, only multi-reference sorting was performed for this dataset.

1.4.5 Atomic Model Building and Refinement

The atomic models of undecorated GMPCPP, GDP and GTPγS-MT were built in COOT [76], based on the high-resolution cryo-EM density maps and our previously deposited atomic models (PDB entries 3JAT, 3JAS and 3JAK for GMPCPP, GDP and GTPγS-MT, respectively) [31]. Torsion angle, planar peptide and Ramachandran restraints were used during the building process in COOT.

For each MT reconstruction, the model of one $\alpha\beta$-tubulin dimer built in COOT was fitted as a rigid-body into the MT lattice to generate an initial model containing 6 tubulin dimers that was subsequently refined with REFMAC v5.8 adapted for cryo-EM [77], following a previously described protocol [31]. Secondary structure and reference restraints generated with ProSMART [78] were used throughout the refinement process. During refinement, local symmetry restraints were used to restrain corresponding interatomic distances in symmetry-related molecules. These local symmetry restraints are functionally analogous to non-crystallographic symmetry (NCS) restraints used during crystallographic refinement [79].

1.4.6 Data Deposition

Data deposition: The cryo-EM maps have been deposited in the Electron Microscopy Data Bank (EMDB) [undecorated GMPCPP-MT (EMD-7973), undecorated GDP-MT GMPCPP-MT (EMD-7974), undecorated GTPγS-MT (EMD-7975), and EB3-washed GMPCPP-MT, class 1 and 2 (EMD-7976 and EMD-7977)]. The refined atomic models for the undecorated GMPCPP-, GDP-, and GTPγS-MT have been deposited in the Protein Data Bank (PBD ID codes 6DPU, 6DPV, and 6DPW, respectively).

1.5 Acknowledgements

We thank Sebastian Maurer for guidance of the assembly of GTPγS-MT in the absence of EBs. We are thankful to Patricia Grob for EM support, and to Tom Houweling and Abhiram Chintangal for computer support. We thank David Bulkley and Alexander Myasnikov for assistance in data collection at UCSF, and James Fitzpatrick and Michael Rau for assistance in data collection at Washington University in St. Louis, Center for Cellular Imaging (WUCCI). This work was funded by a grant from NIGMS (GM051487 to E.N.). B.L. is supported by NSF-GRFP (1106400). E.N. is a Howard Hughes Medical Institute investigator.

Dataset / MT States	GMPCPP	GDP	GMPCPP-K	GTPγS	GMPCPP-EB3	GMPCPP
Location of Data collection	UCSF	UCSF	UCSF	UCB	UCB	WUSTL
Microscope	Titan Krios	Titan Krios	Titan Krios	Titan (low base)	Titan (low base)	Titan Krios
calibrated pixel size	1.079	1.079	1.079	1.330	1.330	1.096
Num of frames	25	25	25	20	20	40
exposure time / frame	0.2	0.2	0.2	0.3	0.3	0.2
Total exposure time (sec)	5	5	5	6	6	8
Dose / frame	1.4	1.4	1.4	1.44	1.44	1.33
Total dose	35	35	35	28.8	28.8	53.2
K2 camera mode	super-resolution	super-resolution	super-resolution	counting	counting	counting
Data collection software	SerialEM	SerialEM	SerialEM	Leginon	Leginon	EPU
Num of Micrographs used	405	695	346	616	182	1176
Num of Particles (13PF / 14PF)	6,465 / 28,882	24,482 / 48,097	5,716 / 29,927	9,071 / 49,145	1,666 / 13,159	25,729 / 110,127
Resolution (symmetrized) (13PF / 14PF)	3.97 / 3.62 Å	3.54 / 3.30 Å	3.82 / 3.50 Å	4.05 / 3.49 Å	(NA / NA) / (4.32 Å / 4.13 Å)	3.43 / 3.11 Å
Resolution (C1) (13PF / 14PF)	4.86 / 4.34 Å	4.12 / 3.90 Å	4.94 / 4.06 Å	5.61 / 4.21 Å	(NA / NA) / (7.05 Å / 4.89 Å)	4.08 / 3.57 Å

Supplemental Table 1.1: Data collection and processing statistics. The resolution number for each reconstruction was estimated by calculating the Fourier Shell Correlation (FSC) of one 'protofilament' containing 3 adjacent tubulin dimers from the odd and even maps, using a FSC 0.143 criterion. For the GMPCPP-EB3 state, the two resolution numbers are for the 14-PF MT and correspond to class 1 and 2, respectively. We did not pursue a reconstruction for the 13-PF MT due to the limited number of segments.

MT States	Intra-dimer Distance	Inter-dimer Distance	Dimer Rise	Dimer Twist
GDP 13-PF	41.44	40.30	81.76	0.08
GDP 14-PF	41.50	40.25	81.74	-0.48
GDP-K 13-PF	41.38	40.36	81.64	0.09
GDP-K 14-PF	41.40	40.20	81.63	-0.46
EB3-GDP 13-PF	41.28	40.24	81.54	-0.13
EB3-GDP-K 13-PF	41.35	40.32	81.59	-0.11
GTPγS 13-PF	41.35	40.45	81.93	-0.12
GTPγS 14-PF	41.32	40.40	81.70	-0.56
EB3-GTPγS 13-PF	41.29	40.32	81.60	-0.25
EB3-GTPγS-K 13-PF	41.31	40.51	81.96	-0.27
GMPCPP 13-PF	41.53	42.43	83.95	0.23
GMPCPP 14-PF	41.56	42.45	83.96	-0.33
GMPCPP-K 13-PF	41.45	42.00	83.30	0.21
GMPCPP-K 14-PF	41.42	41.94	83.29	-0.32
EB3-GMPCPP 13-PF	41.34	40.47	81.98	-0.13
GMPCPP-TPX2 13-PF	41.67	42.61	84.33	0.40
GMPCPP-TPX2 14-PF	41.67	42.56	84.31	-0.23
GMPCPP-EB3 14-PF (class 1)	41.41	40.70	82.25	-0.69
GMPCPP-EB3 14-PF (class 2)	41.55	42.08	83.57	-0.45

Supplemental Table 1.2: Lattice parameters of MTs in different states. The values of the inter-dimer and intra-dimer distances were calculated from the atomic models of each state, using the mean of the Cα distances between α- and β-tubulin for each pair of corresponding residues. The dimer rise and dimer twist were measured from the C1 reconstructions of MTs in different states using the *relion_helix_toolbox* program in RELION v2.1, which gave results consistent with those obtained with the *hsearch_lorentz* program in the IHRSR package that we previously used. To assess the robustness of our measurements, we split the whole dataset for each microtubule sample into three, non-overlapping subsets. The three sets of helical parameters measured from the reconstruction of each subset are then used to calculate the mean value and standard deviation of the helical parameters. For each measurement of dimer rise and dimer twist, the standard deviation is less than 0.02.

Chapter Two

Cryo-EM analysis of catalytically-dead microtubules provides insights into the GTP cap and microtubule instability

Note: With the new-found ability to determine the structure of undecorated microtubules as outlined in the previous chapter, I set out to better understand the role of GTP hydrolysis in microtubule dynamics. Previous studies (aforementioned, and others) have utilized the GTP-analog GMPCPP as a proxy for the GTP state, but no one has ever observed the structure of a GTP-bound microtubule. In order to accomplish this goal, we teamed up with Johanna Roostalu and Thomas Surrey who recently developed an ability to purify recombinant human tubulin. In this study, we create a loss of function mutation in the catalytic residue of tubulin, then use cryo-EM to observe microtubules trapped in the GTP-bound state. Without Johanna and Thomas, these experiments would have been impossible, and much of this chapter is a draft of a manuscript currently under preparation.*

2.1 Abstract

Microtubules are dynamic proteinaceous polymers built from α/β-tubulin heterodimers. A hallmark of microtubules is dynamic instability—rapid switching between growth and catastrophic depolymerization—that is coupled with GTP hydrolysis. GTP hydrolysis is accompanied by conformational changes that are recognized and regulated by a number of microtubule-associated proteins that play crucial roles in the cell. Here we use cryo-EM and recombinant human tubulin that is mutated to prevent GTP hydrolysis in order to better understand the structure of a GTP-bound microtubule and the physiological role of subtle conformational changes in different microtubule states. We find that both catalytically-dead mutants (E254A, and E254N) have an expanded lattice similar to previously observed for porcine GMPCPP-MTs, and that EB proteins have the ability to compact these GTP-bound microtubules. Furthermore, the seam—a weak point in the microtubule lattice—appears to be in a stabilized conformation when bound to GTP, and destabilized when bound to GDP, providing additional mechanistic insight into microtubule dynamic instability.

* Benjamin LaFrance, Basil J Greber, Rui Zhang, Johanna Roostalu, Chloe McCollum, Thomas Surrey, Eva Nogales. *Cryo-EM analysis of catalytically-dead microtubules provides insights into the GTP cap and microtubule instability*. To be submitted to eLIFE.

2.2 Introduction

Microtubules are composed of GTP-bound α/β-tubulin heterodimers that self-assemble into protofilaments and form a cylindrical lattice (Figure 2.1A). During incorporation into the microtubule lattice, GTP hydrolysis occurs and has a destabilizing effect on the overall microtubule structure. Conversely, the GTP-tubulin cap at the growing tip, known as the plus-end of the microtubule, is thought to be a stabilizing agent [26, 80, 81]. Stochastic loss of this GTP-bound cap structure leads to a catastrophic depolymerization event. It has been proposed that GTP islands—stable GTP-tubulin from deep within the microtubule lattice that have evaded hydrolysis— act as a stopgap to prevent further depolymerization, resulting in rescue events [82, 83].

The interplay between the stable GTP-tubulin and meta-stable GDP-tubulin lattices, is a phenomenon known as dynamic instability and is critical to microtubule growth and shrinkage, and thus, microtubule function within the cell [25]. Furthermore, many microtubule-associated proteins such as EBs (end-binding proteins) prefer specific nucleotide states of the microtubule [36, 84-87].

Given the critical nature of the GTP-GDP transition for stability and dynamics within microtubules and the ability of nucleotide-specific recruitment of specialized factors, it is critical to understand the nuanced structural differences between nucleotide states. Previous research on the structure of GTP-tubulin has largely focused on nucleotide analogs. Specifically, cryo-electron microscopy (Cryo-EM) has provided structures of fully formed microtubules with different nucleotide content [31, 32, 88-90], while crystallography has provided structures of polymerization-inhibited tubulin also in different nucleotide states [91-93]. However, the natural structure of the GTP-bound microtubules has not been directly visualized, and it remains unclear which GTP-analog, if any, is an accurate proxy for the GTP microtubule state.

Another important feature of most microtubules is known as the seam. With the exception of the rare 15-protofilament microtubules that have perfect helical symmetry, most other microtubule lattices are pseudo-helical, and contain a seam in order to accommodate the lattice parameters. For seamed microtubules, most interactions across protofilaments are homotypic (α-α or β-β interactions), with one heterotypic interaction (α-β) across adjacent protofilaments at the seam (Figure 2.1A). Given the different interaction interface at the seam, it has often been thought of as a point of weakness [14, 90, 94, 95]. Upon probing microtubules that are bound to GTP-analogs, it appears that the GTP-like microtubule structures are more circular in cross section than their GDP-like counterparts [90]. Whether this holds up for true GTP microtubule segments remains to be seen.

Here, cryo-EM was used to observe microtubules formed from catalytically-dead recombinant human tubulin in order to better understand microtubules in the GTP conformation. Furthermore, we looked at these microtubules in the presence and absence of end-binding proteins (EB3), to clarify why EB3 preferentially binds the microtubule end. We found that wild-type recombinant microtubules are structurally

indistinguishable from the endogenous microtubules previously described. Catalytically-dead microtubules are markedly similar to GMPCPP microtubules in terms of lattice parameters with a few notable exceptions. Strikingly, it appears that microtubule compaction can occur without GTP hydrolysis, as seen for catalytically-dead MT+EB3 structures. Furthermore, it appears that the regularized seam hypothesis proposed for stable GTP-like microtubules [90] also holds true for catalytically dead microtubules that are trapped in a GTP-bound state. These structures inform our understanding of the pre-hydrolysis state of microtubules, help explain the preference of EB3 for certain microtubule states, and provide additional insights into the intrinsic regulation of microtubule instability.

2.3 Results & Discussion

In order to better understand how GTP hydrolysis affects the microtubule structure, we sought to structurally characterize microtubules (MTs) assembled from catalytically-dead tubulin, which are constitutively locked in the GTP state. Recombinant human tubulin was purified and biochemically characterized as described previously [96] and then visualized by cryo-EM. Initially, wild-type recombinant human tubulin acted as a control to confirm that the purification tags necessary for the recombinant system did not alter the MT structure. Subsequently, catalytically dead mutants that prevent GTP hydrolysis were used as a proxy to look at a GTP-like MT conformation. Specifically, these mutants abolish the catalytic glutamate at residue 254 (E254A, E254N). For the purposes of this study, 13-protofilament (13pf) microtubules were extensively characterized, given their abundance and direct physiological relevance in mammalian cells [4, 97, 98]. It is worth noting that the characteristics of 13pf MTs described in this work held true for the 14pf MTs also observed.

2.3.1 Wild-type recombinant tubulin does not alter the MT architecture

Wild-type (E254E) tubulin polymerized into MTs with lattice parameters as expected for a hydrolysis-competent GDP MTs (MTs in which GTP is hydrolyzed during polymerization; Figure 2.1D and Table 2.1). Structurally, the E254E-MTs, both undecorated and decorated with kinesin, were indistinguishable from previously reported mammalian GDP-MT structures [32, 90], with the exception of additional density corresponding to the internal His_6-tag located within the disordered acetylation loop of alpha-tubulin at residue K40 (Figure 2.1B,C). The purification tags have no effect on polymerization dynamics [96], nor do they alter lattice parameters compared to endogenous wild-type porcine microtubules studied previously (Table 2.1).

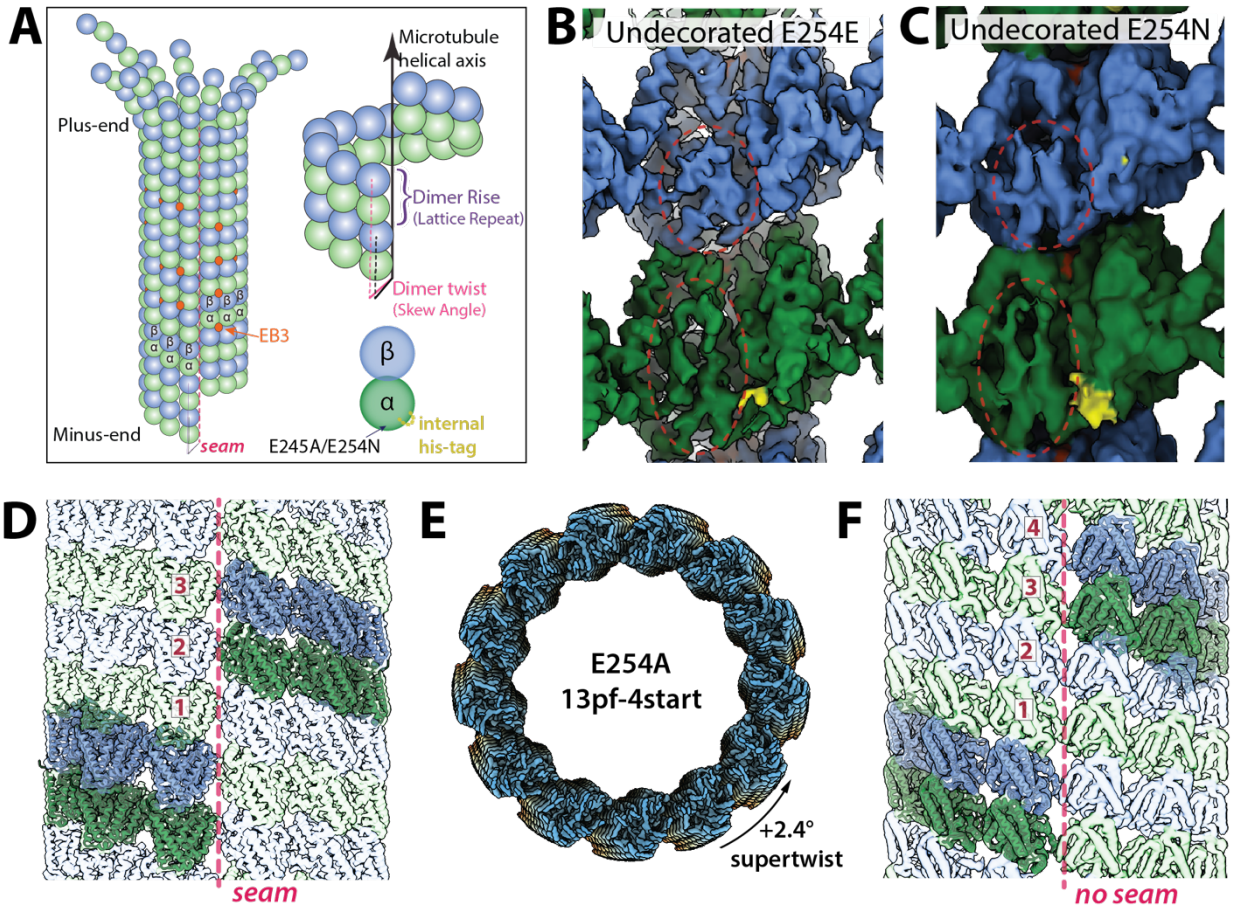

Figure 2.1 High-resolution structure of undecorated mutant MTs. (A) Cartoon diagram of a 13pf 3-start MT undergoing depolymerization, with α-tubulin in green, β-tubulin in blue, and EB3 in orange (colors maintained throughout). Also shown are the dimer rise and dimer twist (or skew angle) of the MT lattice, where rise denotes the distance (in Å) from one tubulin dimer to the one directly above it and twist is the angle around the MT helical axis that must occur going from one dimer to the one above. A twist=0° would indicate that tubulin dimers are stacked perfectly vertical with respect to one another (i.e. that the protofilaments run perfectly parallel to the MT axis). View of tubulin dimers from the lumen, where red circles highlight distinctive features of the α/β subunits as seen for undecorated MTs for E254E **(B)** and E254N **(C)**. The small density highlighted in yellow is a result of the internal His_6-tag. **(D)** A traditional 13pf 3-start MT (in this case, undecorated E254A). The same generic architecture was observed for E254E, and E254N (though with subtle differences in lattice parameters). However, sub-classification of all 13pf E254A particles revealed a subset of 13pf 4-start particles; colored blue-yellow-orange along the MT-axis to show depth in **(E)**, and from the side in **(E)**. In (C) and (E) one helical layer of tubulin dimers is highlighted to stress the two different, with corresponding ribbon diagrams docked into the dimers.

2.3.2 A comparison between E254A MTs and GMPCPP MTs

For the catalytically dead mutant E254A, traditional cryo-EM processing protocols [1, 99] failed to yield a high-resolution structure. Instead, the E254A reconstruction appeared smeary and had an abnormally large twist parameter of +0.88°, which was clearly visible even in 2D class averages (Supplemental Figure 2.1). In order to achieve higher resolution, further 3D classification was necessary beyond the initial classification by protofilament number. After 2 rounds of sub-classification, it became clear that there were at least two specific lattice conformations for 13pf E254A MTs, explaining the low resolution of the averaged cryo-EM maps. Unexpectedly, both a 13pf 3-start and a 13pf 4-start lattice were observed (Figure 2.1D-F). The 13pf 3-start structure had similar lattice

parameters to those previously described for a GMPCPP-bound MT, with a dimer rise of 83.18 Å corresponding to an expanded lattice, and a twist of -0.21° (Table 2.1). Historically, 4-start lattices have been exclusive to 15pf and 16pf MTs, and very rarely, 14pf [100]. Similar to the 13pf 3-start MT, the 13pf 4-start lattice was also in the expanded conformation, with a dimer repeat of 83.03 Å. Furthermore, the 4-start lattice appeared to have the same lateral contacts as the 3-start lattice, with the exception that all 4-start contacts were homotypic (truly helical and without a seam) and the 13pf 3-start MTs displayed the canonical heterotypic seam.

2.3.3 Non-canonical start-numbers for GTP-bound MTs

Different start number lattices have been extensively characterized by Chretien *et al*, but start number switching is rare for 13pf MTs [100]. Of note, the 13pf 4-start phenomenon has also been observed recently in a GDP-BeF_3^- analog [91], but was not analyzed further. The unexpected lattice plasticity of these MTs may indicate increased flexibility of the GTP-bound state. It is possible that flexibility in the MT lattice could play a functional role during the early stages of MT formation. Furthermore, the defects introduced in these different lattice types may act as an internal modulator of MT dynamics. Alternatively, the 13pf 4-start structure may also be a specific characteristic of the experimental system used here, possibly because of artificial protofilament tilting caused by the cavity-creating alanine mutation, similar to what has been diagramed previously (figure 5A from Zhang et al, 2018).

2.3.4 E254N MTs behave much more similarly to GMPCPP MTs than their E254A counterpart

To address the possibility of the cavity-creating mutation having an effect in itself, we analyzed a less drastic E254N mutation. For the E254N MTs, we did not detect any 13pf 4-start MT species. In fact, the 13pf E254N MTs were remarkably similar to previously observed porcine GMPCPP MTs, with a dimer repeat of 83.45Å and a twist of +0.13° (Table 2.1). For GMPCPP MTs, the lattice has a rise of 83.95Å, and a twist of +0.23°.
Furthermore, comparison of backbone carbon deviations between E254N and either GMPCPP-MTs or GDP-MTs clearly shows the E254N and GMPCPP similarity (Supplemental Figure 2.2). Thus, the structure of a true GTP-bound E254N mutant MT determined here validates the use of wild-type GMPCPP MTs for structural analysis. These results also indicate that E254A may not be the ideal substrate for future *in vivo* and *in vitro* studies. The fact that the tubulin residues critical for hydrolysis also provide interactions at the polymerization interface makes the design of catalytically-dead MTs very sensitive to subtle changes.

2.3.5 Expanded lattices as a proxy for the GTP-bound MT

In previous years, high-resolution cryo-EM structures have used GMPCPP as a proxy for the GTP, and that microtubules go from an expanded to compacted state following the GTP to GDP transition. However, many other GTP-analogs have not been explored to confirm this hypothesis, as recently discussed by Estevez-Gallego *et al [91]*. Their x-ray crystallographic structures of both GDP-AlF_x and GDP-BeF_3^- analogs have given rise to

a different model where GDP-BeF_3^- MTs are compacted, and undergo expansion specifically during the transition state in order to release inorganic phosphate (seen for GMPCPP, GMPCP, and GDP-AlF_x), followed by a compacted GDP state. In this scenario, it is the methylene linkage present in GMPCPP that is responsible for the expanded conformation. However, it is worth noting that the experimental requirements of crystallographic structure determination (polymerization-inhibited bent conformations) cause significantly larger perturbations on the tubulin structure than a methylene linkage. This unfortunately makes the data difficult to relate to a more physiological sample. Similarly, the MT structures presented here require mutations to constitutively-lock tubulin in a GTP state, and these mutations can have significant consequences on MT structure (as seen for the E254A mutant).

Although there remains uncertainty in the field regarding the specific conformational changes sampled by a MT throughout GTP hydrolysis, there is an abundance of evidence that both a compacted and expanded state have significant biological relevance. Expanded lattices have been observed in both *S. cerevisiae* and *S. pombe*, and numerous MAPs can modulate dimer rise parameters [101-103]. Taken together, it is increasingly clear that there is a need to overcome the technical limitations in order to identify and characterize the GTP-state in a native dynamic sample.

Sample	Lattice Spacing/ Dimer Rise (Å)	Skew/ Twist (°)	Intradimer Rise (Å)	Interdimer Rise (Å)	Reference
GMPCPP-TPX2	84.33	+0.40	41.67	42.61	Zhang et al, 2018
GMPCPP	83.95	+0.23	41.53	42.43	Zhang et al, 2018
GMPCPP-DCX	83.74	+0.16	NA	NA	Manka et al, 2018
GMPCPP-Kinesin	83.16	+0.19	41.45	42.00	Zhang et al, 2018
E254N	**83.45**	**+0.13**	**41.53**	**41.93**	**This Study**
E254A 3-start	**83.18**	**-0.22**	**NA**	**NA**	**This Study**
E254A 4-start	**83.03**	**+2.40**	**NA**	**NA**	**This Study**
GDP-P_i-DCX	81.74	0.00	NA	NA	Manka et al, 2018
GTPγS-K-EB3	81.96	-0.28	41.31	40.51	Zhang et al, 2018
GTPγS	81.93	-0.12	41.35	40.45	Zhang et al, 2018
GTPγS-EB3	81.52	-0.25	41.30	40.30	Zhang et al, 2015
GTPγS-DCX	82.10	-0.02	NA	NA	Manka et al, 2018
GDP-DCX	81.90	+0.08	NA	NA	Manka et al, 2018
GDP	81.76	+0.08	41.44	40.30	Zhang et al, 2018
E254E-Kinesin	**81.69**	**-0.09**	**41.38**	**40.37**	**This Study**
GDP-Kinesin	81.64	+0.01	41.38	40.36	Zhang et al, 2018
GDP-K-EB3	81.59	-0.11	41.35	40.32	Zhang et al, 2018
E254E	**81.50**	**0.05**	**41.25**	**40.30**	**This Study**
GDP-EB3	81.44	-0.12	41.40	40.3	Zhang et al, 2015
E254N-EB3	**81.15**	**-0.29**	**NA**	**NA**	**This Study**
E254A-EB3	**81.12**	**+0.21**	**41.42**	**40.47**	**This Study**

Table 2.1. Lattice parameters for select 13pf microtubule structures. Lattice parameters for microtubules in this study are reported alongside previously published structures for reference. Expanded lattices are in yellow (GMPCPP

and undecorated catalytically-dead mutants); presumed transition state microtubules (GDP+P_i or GTPγS) are colored in green, and compacted lattices are shaded in blue (GDP state, or catalytically-dead mutants + EB3). NA signifies cases where intra-dimer or inter-dimer was not reported, where it was not reliable due to mixing of α/β-tubulin subunits, or where resolution was too low to accurately determine the values.

2.3.6 EB3 compacts both E254A and E254N MTs

The MT-associated protein EB3 is a commonly used tool to track the growing GTP-cap at the fast growing plus-end of MTs, (the end that exposes the β-tubulin subunit—Figure 1A, top—) and also has the ability to promote compaction and induce GTP hydrolysis ([31]). We therefore sought to see what effect EB3 could have on mutant MTs that were locked in a GTP-bound state. Addition of EB3 to E254A MTs caused the microtubule dimer repeat to decrease from 83.13Å to 81.12Å, indicative of a lattice compaction toward a conformation toward a GDP-like conformation (Table 2.1, Figure 2.2). This same compaction phenomenon was observed for the E254N MTs in the presence of EB3, although EB3 occupancy was significantly lower. Lower EB3 occupancy for E254N agrees with the biochemical data (personal communication with Thomas Surrey). Interestingly, the high resolution EB3-bound catalytically-dead MT structure clearly shows that GTP is still present in the active site while the MT is sampling the compacted GDP-like lattice (Figure 2.2D). Previous structures of MTs decorated with EB3 have showed a dimer twist of around -0.3° [31, 90]. This agrees well with what was observed for the E254N+EB3 MTs (-0.29°), but the twist for E254A+EB3 MTs was found to be +0.21°. This difference could again be due to an effect of the cavity-creating mutation. However, the E254A+EB3 MT map was reconstructed from a relatively small dataset, we cannot discard the possibility that the different dimer twist for this species may be explained by a residual amount of 13pf 4-start MTs, as was shown within the much larger dataset for undecorated E254A MTs.

2.3.7 Microtubule compaction can occur without GTP hydrolysis

One outstanding question in the field is whether MT lattice compaction causes the hydrolysis of GTP, or if hydrolysis and/or the release of inorganic phosphate allows space for the compaction to occur. The data presented here show that EB3 has the ability to compact a lattice where GTP is definitively present. This finding suggests an order-of-operations in which bringing the catalytic reside on one side of the interface close to the nucleotide facilitates hydrolysis. Once hydrolysis and/or Pi release occurs, it is energetically favorable for the lattice to remain in the compacted state. Although in principle, the compacted E254A+EB3 structure might be a consequence of the cavity-creating alanine mutant, this interpretation is far less likely to be true for the E254N+EB3 structure, which lacks such a cavity but is also compacted. These data are in line with other growing evidence in support of a lattice-centric model for MTs [15, 104], where the GTP hydrolysis is induced by the lattice conformation.

Recent biochemistry has shown that EB3 has an extremely high binding affinity for the E254A mutant, and a lower affinity for the E254N mutant, with a cooperative switch to a higher binding state (personal communication with Thomas Surrey). Although, both a low and high affinity state were observed for E254N in biochemical experiments, under the

conditions used for cryo-EM, we could not identify multiple different states of EB3-binding. For E254A-MTs, the extensive analysis required to classify specific structural states was largely due to the heterogeneity regarding the dimer twist parameter. This indicates that E254A has a greater structural plasticity compared to E254N-MTs or GMPCPP-MTs. Given that EB3 modifies the twist parameter in order to bind MTs, it may be that the flexibility of the E254A-MT species provides a lower energy barrier for the conformational changes required upon EB3 binding. Additionally, the more abundant 13pf 3-start helix found in the undecorated E254A dataset has a dimer twist of -0.22° which is very similar to the dimer twist induced by EB3 binding. This twist indicates that a percentage of the undecorated E254A MTs may be pre-programmed with the lattice parameters preferred by EB3. Taken together with the conformational plasticity of the E254A mutant, these results help explain the extremely high affinity between E254A MTs and EB3.

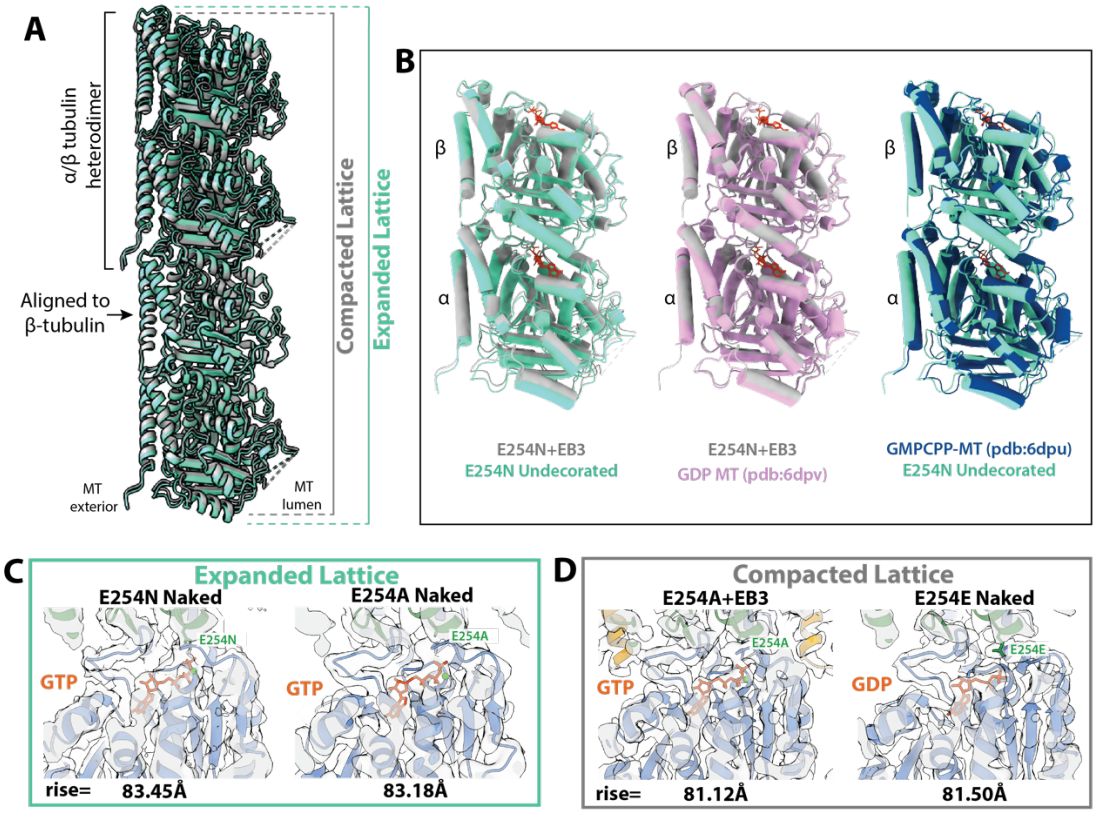

Figure 2.2 Compaction and nucleotide state for various catalytically-dead MTs. Visualization of how the lattice parameters change upon MT maturation is shown in **(A)**, either through hydrolysis of GTP, or through EB3 binding to catalytically dead MTs. Specifically shown here are refined PDB coordinates docked into the undecorated E254N MT map in cyan, and E254N-EB3 MT map in grey. In panel **(B)**, tubulin heterodimers are compared to show the structural changes that occur upon compaction. Expanded lattices, with a rise >83Å and with clear GTP density are in **(C)**, whereas compacted lattices with a rise <82Å in **(D)** can be formed by EB3 binding (while maintaining GTP), or by hydrolysis into the GDP state.

2.3.8 The seam is closed for GTP-bound MTs, and opens upon GTP hydrolysis

During MT formation, it is generally accepted that individual tubulin dimers undergo a certain amount of strain to accommodate the lattice architecture. This strain then manifests as potential energy in which individual tubulin dimers act as loaded springs

within the MT lattice. Due to the heterotypic α/β interactions formed across the seam, the has been seam considered a potential weak point of the MT lattice. For the E254N structure, all protofilaments are regularly arranged in an almost perfectly circular cross-section around the MT axis (Figure 2.3B) as is clearly shown when calculating displacement values between a symmetrized and a C1 reconstruction [90]. For E254E MTs, the protofilaments interacting at the seam are clearly displaced outward from each other with respect to the relative position of all other protofilaments, regardless of the presence or absence of kinesin (Figure 2.3C, D). We see that the E254E seam is more open than the GTP-like E254N MT. Unfortunately, due to the extensive processing required to determine a structure for the undecorated E254A mutants, we were unable to bootstrap on previous protocols to determine the seam. Consequently, the seam analysis was not possible for this dataset. However, addition of EB3 to E254A MTs enforced EB3's preferred MT conformation and regularized the protofilaments, as expected (Figure 2.3A).

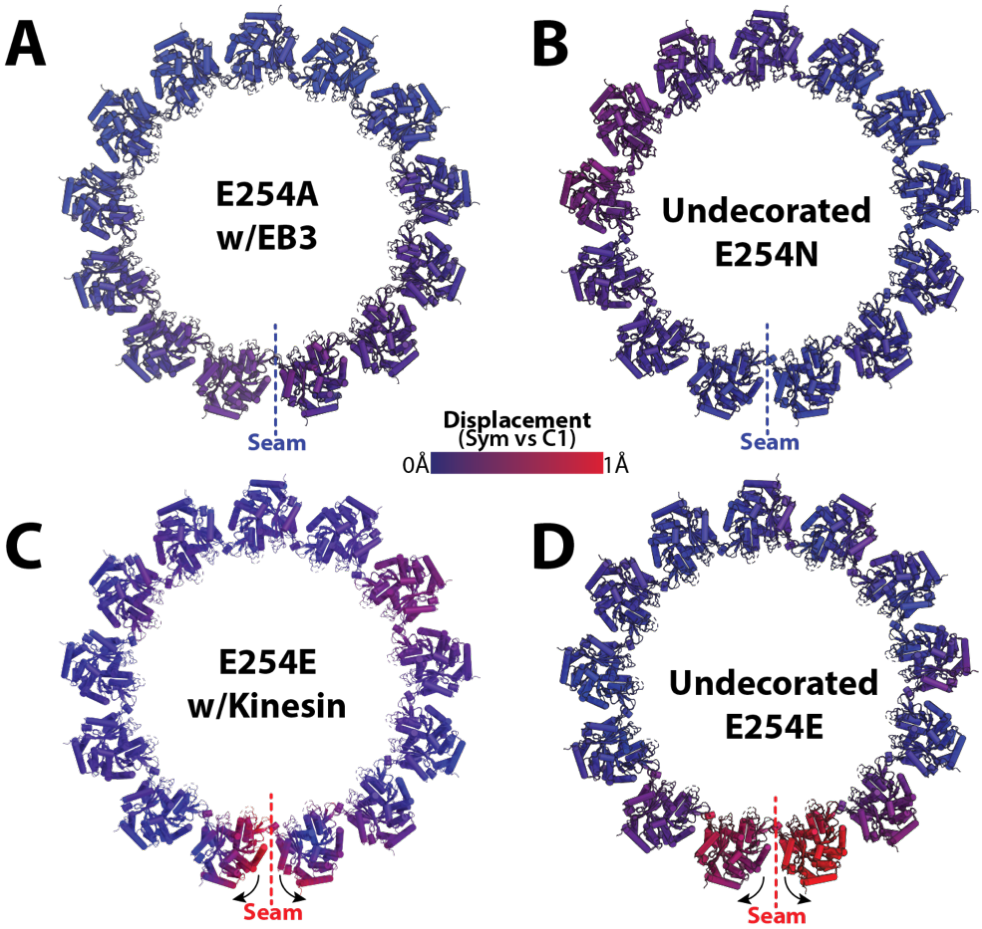

Figure 2.3 Microtubule cross-section of a MT for both GTP-like and GDP-MTs. Comparison between the symmetrized and C1 maps shows a highly symmetric circular MT for E254A+EB3 MTs **(A)**, and for GTP-bound E254N MTs (**B)**. MTs in a post-hydrolysis GDP state showed large displacement localized to the protofilaments at the seam **(C)** and **(D)**. Supplemental Video 1 allows for a dynamic visualization of this motion.

2.3.9 The microtubule seam serves as a proxy for MT instability

The GTP cap of GTP-containing tubulin subunits at the plus-end of a MT has long been thought of as a stabilizing agent [26, 105]. Catastrophic depolymerization events occur when this GTP cap is lost. What is the nature of this lattice destabilization upon exposure of GDP-containing subunits? We have previously proposed that the tension present in the GDP-lattice can be directly visualized as a seam-opening phenomenon, that appears to localize and have the greatest effect at the GTP-to-GDP transition zone. This model was put forward considering that GMPCPP gives rise to a GTP-like MT lattice. We believe that the present study, using hydrolysis mutants instead of GTP analogs, further support such model.

A recent, more localized analysis by the Sindelar group, revealed a surprising large amount of flexibility in protofilament orientation relative to one another at all pf locations [106]. We believe that some of these dynamics may also be present in our MT samples, albeit to a lesser extent than taxol MTs. However, our analyses average out these localized fluctuations. The fact that the averaged seam location is distinct for different nucleotide state, indicates the robustness of the seam-opening phenomenon.

Given the highly circular and symmetric protofilament orientation along the MT axis observed for the E254N mutant (Figure 3B), and the same phenomenon observed for GMPCPP MTs, we propose that this symmetry is associated with the stability of the GTP region of MTs. Similarly, the symmetry-breaking outward rotation of the seam-proximal protofilaments in the E254E microtubules, as well as porcine GDP MTs, reflects the weakening of the seam upon hydrolysis that likely precedes protofilament peeling and depolymerization. This molecular mechanism should hold true for all seam containing MTs, which are the overwhelming majority.

2.4 Conclusions

The recent ability to purify recombinant MTs has allowed us to further probe the GTP conformation of microtubules by creating catalytically dead mutants that constitutively lock MTs in a GTP state. The wild-type (E254E) recombinant MTs appear very similar to previously observed mammalian MTs [90]. It will be exciting to see how this platform is utilized in the future to probe MT function (ie, phosphomimetic mutants, key interfaces, etc). In this work, we utilized recombinant MTs to better understand GTP hydrolysis. The fact that EB3 has the ability to compact GTP-bound MTs, indicates that compaction likely occurs before hydrolysis, an observation that has been seen elsewhere in the literature recently [91]. Surprisingly, it appears that an E254A mutation allows for a conformational plasticity such that 13pf MTs can sample both a 3-start and 4-start helix. These mutational studies have provided additional evidence regarding the stability at the seam, where MT cross-sections are highly symmetrized for GTP-bound mutants as well as GMPCPP [31, 90], and the seam opens upon hydrolysis as seen for the GDP-bound structures. Although the unperturbed GTP-bound structure of MTs remains elusive, these mutants provide additional insights into the instability and conformational dynamics that accompany the GTP-to-GDP transition for microtubules.

2.5 Materials and Methods

2.5.1 Purification of Recombinant Human Tubulin

Human tubulin was purified recombinantly as described previously [96]. Briefly, cell pellets from 2 liters of High Five insect cells expressing human TUBB3-TEV-Strep and TUBA1B-His^{internal} (WT, E254A, or E254D) were resuspended 1:1 (v/v) in cold lysis buffer and lysed by douncing 60 times. Lysate was diluted 4-fold in dilution buffer, and clarified by ultracentrifugation (158,420x g, 1 hr, 4°C). The supernatant was passed through a HisTrap HP column (GE Healthcare), and the elution was immediately diluted 6x in Strep buffer, and passed through a 1mL HiPrep column followed by a 5mL StrepTag HP column. Tubulin was eluted off the column, diluted 2-fold in Strep elution buffer and incubated on ice for 2 hours with TEV protease to remove the Strep-TagII from TUBB3. The eluate was then clarified by ultracentrifugation (204,428x g, 10min, 4°C). The supernatant was further purified through a 1mL HiPrep SP FF column, desalted into storage buffer, concentrated to 3.5mg/mL, ultracentrifuged (278,088x g, 10min, 4°C), and flash frozen in 10uL aliquots with liquid nitrogen.

Lysis	80mM PIPES, 1mM EGTA, 6mM $MgCl_2$, 50mM imidazole, 100mM KCl, 2mM GTP, 1mM BME, pH 7.2 + protease inhibitors and DNAse
Dilution	80mM PIPES, 1mM EGTA, 6mM $MgCl_2$, 50mM imidazole, 2mM GTP, 1mM BME, pH 7.2
His Elution	80mM PIPES, 1mM EGTA, 5mM $MgCl_2$, 500mM imidazole, 2mM GTP, 1mM BME, pH 7.2
Strep Binding	80mM PIPES, 1mM EGTA, 5mM $MgCl_2$, 2mM GTP, mM BME, pH 7.2
Strep Elution	80mM PIPES, 1mM EGTA, 4mM $MgCl_2$, 2.5mM D-desthiobiotin, 50mM imidazole, 2mM GTP, 1mM BME, pH 7.2
Storage	80mM PIPES, 1mM EGTA, 1mM $MgCl_2$, 0.2mM GTP, pH 6.8

2.5.2 Purification of EB3

Monomeric EB3 was purified as previously described [31, 36]. Human $EB3_{1-200}$ was inserted into a 2BT vector with a C-terminal HisTag (Macrolab, UC-Berkeley), and expressed in BL21(DE3)-RIL *E. coli*. Cell pellets from a 2L culture were resuspended in 1:2 (v/v) Lysis Buffer, and lysed by sonication. Cell debris was pelleted by centrifugation (18,000x g, 45min, 4°C), and supernatant was loaded on a 5mL HisTrap column (GE Healthcare), and eluted with a 0-100% gradient of Lysis buffer to elution buffer. The elution was incubated with TEV protease overnight at 4°C to remove the HisTab, followed by a subtractive nickel purification to remove TEV, uncleaved EB3, and the HisTag. Flowthrough was concentrated to 500uL and loaded on a Superdex 200 10/300 GL pre-equilibrated in SEC buffer for size-exclusion chromatography. Peak fractions were pooled, concentrated to 20uM, and flash frozen in SEC buffer until needed.

Lysis	50mM Tris pH 8.0, 150mM NaCl, 1mM EDTA, 1mM DTT + protease inhibitors, DNAse, RNase, and Lysozyme
His Elution	50mM Tris pH 8.0, 150mM NaCl, 1mM EDTA, 1mM DTT, 300mM imidazole
SEC Buffer	50mM Tris pH 8.0, 150mM NaCl, 1mM EDTA, 1mM DTT, 10% glycerol

2.5.3 Purification of Kinesin

The kinesin plasmid was generously supplied by the Vale lab [107], and purified as described previously [32]. The plasmid encoding His_6-tagged, monomeric, catalytically-dead Kif5b (1-350aa, E236A) was transformed into BL21(DE3) cells for expression. Upon reaching OD_{600}=0.5, the 1L expression culture was reduce to 22°C, and induced with 0.2mM IPTG for 16 hrs. The cells were harvested with by centrifugation at 4000g for 20min at 4°C. Cell pellets were resuspended in Lysis Buffer and incubated at room temperature for 30min followed by sonication (3x45sec, at power level 7). The lysate was clarified by centrifugation at 30,000g for 60min, and the supernatant was then incubated with Nickel-NTA beads (GE Healthcare). The protein was washed with 6 column volumes of wash buffer, and eluted with 2 column volumes of elution buffer. The elution was pooled and loaded onto a size exclusion column equilibrated with SEC buffer. Fractions were analyzed by SDS-PAGE for kinesin, and peak fractions were pooled and concentrated to 20uM before flash freezing in liquid nitrogen until needed.

Lysis	50mM $NaPO_4$ pH 8.0, 300mM KCl, 2mM $MgCl_2$, 10% glycerol, 10mM Imidazole, 1mM DTT
Wash	50mM $NaPO_4$ pH 8.0, 150mM KCl, 2mM $MgCl_2$, 10% glycerol, 30mM Imidazole, 1mM DTT, 200uM ATP
Elution	50mM $NaPO_4$ pH 8.0, 150mM KCl, 2mM $MgCl_2$, 10% glycerol, 250mM Imidazole, 1mM DTT
SEC buffer	25mM Tris pH 7.5, 150mM KCl, 10% glycerol, 2mM $MgCl_2$, 2mM DTT

2.5.4 Cryo-EM Sample Preparation

CryoEM specimens were prepared on CFlat 1.2/1.3-T open hole grids (Protochips) that were plasma cleaned for 30 seconds with a Tergeo plasma cleaner (Pie Scientific). A 10uL aliquot of tubulin was thawed on ice for 10min and supplemented with 0.05% NP-40. The tubulin was incubated at 37°C for 30-40min to form microtubules. While polymerizing, the Vitrobot Mark IV was equilibrated to the following conditions: 37°C, 100% humidity, 15 blot force, and a 4 second blot with 1 second drain time. 2uL of microtubule solution was adsorbed onto the grid for 30 seconds, followed by plunge freezing into a eutectic solution of liquid ethane/propane (70:30). For conditions where Kinesin or EB3 were used to decorate the microtubule, two 4uL aliquots of 20uM kinesin/EB3 were added to the microtubule grid with a 30 second wait time in between additions to allow binding. Blotting conditions were identical for all mutants and decorating proteins MAPs to maintain consistency.

2.5.5 Cryo-EM Data Collection

All grids were clipped and loaded into a Gatan Autoloader for imaging at the BACEM Titan Krios microscope at UC-Berkeley. The data was collected with a GIF energy filter and Gatan K2 or K3 camera (depending on the dataset) operating in super-resolution mode. Data collection was controlled by SerialEM [108]. Each micrograph had a total electron exposure of $40e^-$ collected over 40 frames and was collected within a defocus range of 0.8-2.0um. For more specific parameters for each dataset please see Supplemental Table 2.1. The E254A structure was obtained over 2 different data collection sessions

because a more thorough classification was necessary. It should be noted that the same grid was used for both sessions, and there was no bias in the number of the 13pf 4-start particles for either of the data collections.

2.5.6 Cryo-EM Analysis and Model Building

After data collection, processing was done mostly within the RELION framework [109]. Final processing steps that are specific to microtubules were performed in FREALIGN which was necessary for identifying the correct seam location for undecorated microtubules [73]. Briefly, MotionCorr 2.1 5x5 patch-based alignment was performed on each micrograph [69]. CTFFind4 was used to estimate the defocus each micrograph [110]. Microtubules were manually picked within RELION, and extracted with a repeat length of 82Å. Initial protofilament classification was performed with RELION's Class3D function on bin4 data. Once the helical parameters were classified, particles within the same class (primarily 13 protofilament) were unbinned, re-centered, and re-extracted. Unbinned particles were refined within RELION, and then converted into FREALIGN format for pseudo-helical Fourier symmetrization to improve resolution, as well as SeamSearch protocols [1] to correctly identify the seam location. Specific processing pipelines can be found in Supplemental Figure 2.2.

Atomic models were built using a previous porcine microtubule structure as a template (pdb: 6dpu), changing the necessary residues to accommodate differences between porcine and human tubulins as well as the active site mutations. Each tubulin subunit was rigid-body docked with phenix, and refined using the real space refinement program within PHENIX [111, 112]. All refinements were treated with the same number of iterations in order to minimize variation in the processing pipeline.

For the seam analysis, atomic coordinates were rigid-body docked into both the C1 and pseudo-helical symmetry refined maps. The displacement was calculated using the *colorbyrmsd.py* script within PyMol (PyMOL Molecular Graphics System, Schrödinger LLC) and then normalized so that all samples were on the same scale from 0-1 Å.

2.6 Acknowledgements

We would like to thank A Chintangal and P Tobias for support with computation, as well as DB Toso, J Remis, and P Grob for support with microscopy. This work was funded in part by NIGMS (GM051487 to EN). BL was supported by an NSF-GRFP grant 1106400, and EN is a Howard Hughes Medical Institute Investigator.

2.7 Accession Codes

The following cryo-EM maps and refined atomic models will be deposited in the Electron Microscopy Data Bank and Protein Databank: E254E undecorated (EMD-XXXX, PDB-XXXX); E254E+kinesin (EMD-XXXX, PDB-XXXX); E254A 3/4-start (EMD-XXXX); E254A+EB3 (EMD-XXXX, PDB-XXXX); E254N undecorated (EMD-XXXX, PDB-XXXX); and E254N+EB3 (EMD-XXXX).

Supplemental Table 2.1 Data collection, 3D reconstruction, and refinement statistics.

Dataset	**E254E**	**E254E+kin**	**E254A (3/4)**	**E254A+EB3**	**E254N**	**E254N+EB3**
Microscope	Titan Krios	Titan Krios	Titan Krios	Titan Krios	Titan Krios	Titan Krios
Stage type	Autoloader	Autoloader	Autoloader	Autoloader	Autoloader	Autoloader
Voltage (kV)	300	300	300	300	300	300
Detector	Gatan K2	Gatan K2	Gatan K3	Gatan K2	Gatan K3	Gatan K3
Data Collection Software	SerialEM	SerialEM	SerialEM	SerialEM	SerialEM	SerialEM
Acquisition mode	Super-res	Super-res	Super-res	Super-res	Super-res	Super-res
Physical pixel size (Å)	0.575	0.460	0.595	0.460	0.575	0.575
Defocus range (μm)	0.5-2.5	0.7-2.4	0.6-2.5	0.5-2.5	1.0-2.7	1.0-2.7
Electron exposure (e^-/A^2)	40	40	40	40	40	40
Reconstruction	**EMD-XXXX**	**EMD-XXXX**	**EMD-XXXX**	**EMD-XXXX**	**EMD-XXXX**	**EMD-XXXX**
Session	18Dec07b	18Dec07c	19Jun03	18Oct01a	20Feb03	20Feb04
Software	RELION 3.1 & Frealign	RELION 3.1 & Frealign	RELION 3.1 & Frealign	RELION 3.1 & Frealign	RELION 3.1 & Frealign	RELION 3.1 & Frealign
Particles picked	33,575	39,703	165,039	32,107	77,703	6,465
Particles final (13pf)	19,365	23,264	13_3: 68000 13_4: 26022	10,008	13,706	3,825
Extraction box size (pixels)	512^3	512^3	512^3	512^3	512^3	256^3
Final pixel size (Å)	0.92	0.92	1.19	0.92	1.15	2.30
Map resolution (Sym; Å)	3.8	3.6	13_3: 3.4 13_4: 3.7	3.8	3.8	5.0
Map sharpening B-factor ($Å^2$)	-88	-92	13_3: -38 13_4: -50	-118	-36	-100
Coordinate refinement						
Software	PHENIX	PHENIX	--	PHENIX	PHENIX	--
Refinement algorithm	REAL SPACE	REAL SPACE	--	REAL SPACE	REAL SPACE	--
Resolution cutoff (Å)	3.8	3.8	--	3.8	3.8	--
$FSC_{model\text{-}vs\text{-}map}$=0.5 (Å)	3.9	4.0	--	4.0	4.2	--
Model	**PDB-XXXX**	**PDB-XXXX**	**--**	**PDB-XXXX**	**PDB-XXXX**	**--**
Number of residues	864	864	--	995	861	--
B-factor overall	115	92	--	113	120	--
R.m.s. deviations						
Bond lengths (Å)	0.006	0.005	--	0.006	0.004	--
Bond angles (°)	0.606	0.563	--	0.576	0.545	--
Validation						
Molprobity clashscore	12.57	11.81	--	10.3	13.43	--
Rotamer outliers (%)	5.4	5.9	--	5.3	5.8	--
C_β deviations (%)	0.0	0.0	--	0.0	0.0	--
Ramachandran plot						
Favored (%)	95.2	95.7	--	95.0	95.0	--
Allowed (%)	4.8	4.3	--	5.0	5.0	--
Outliers (%)	0.0	0.0	--	0.0	0.0	--

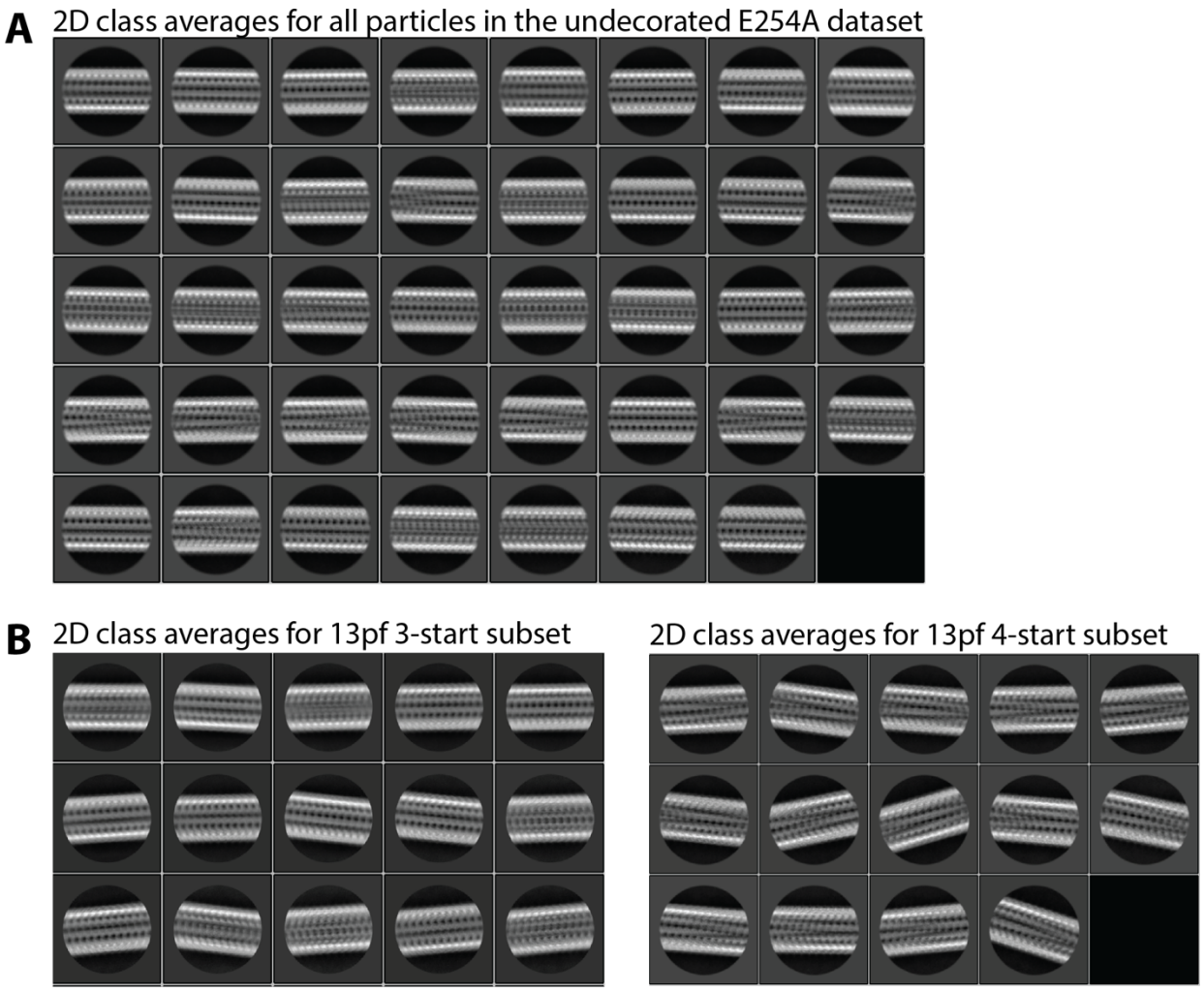

Supplemental Figure 2.1 I 2D class averages obtained during the undecorated E254A MT processing pipeline. **(A)** shows the 2D classification results obtained from the entire dataset. After classification into protofilament type, and additional sub-classification within protofilament, both straight classes (left) and super twisted classes (right) where observed **(B)**.

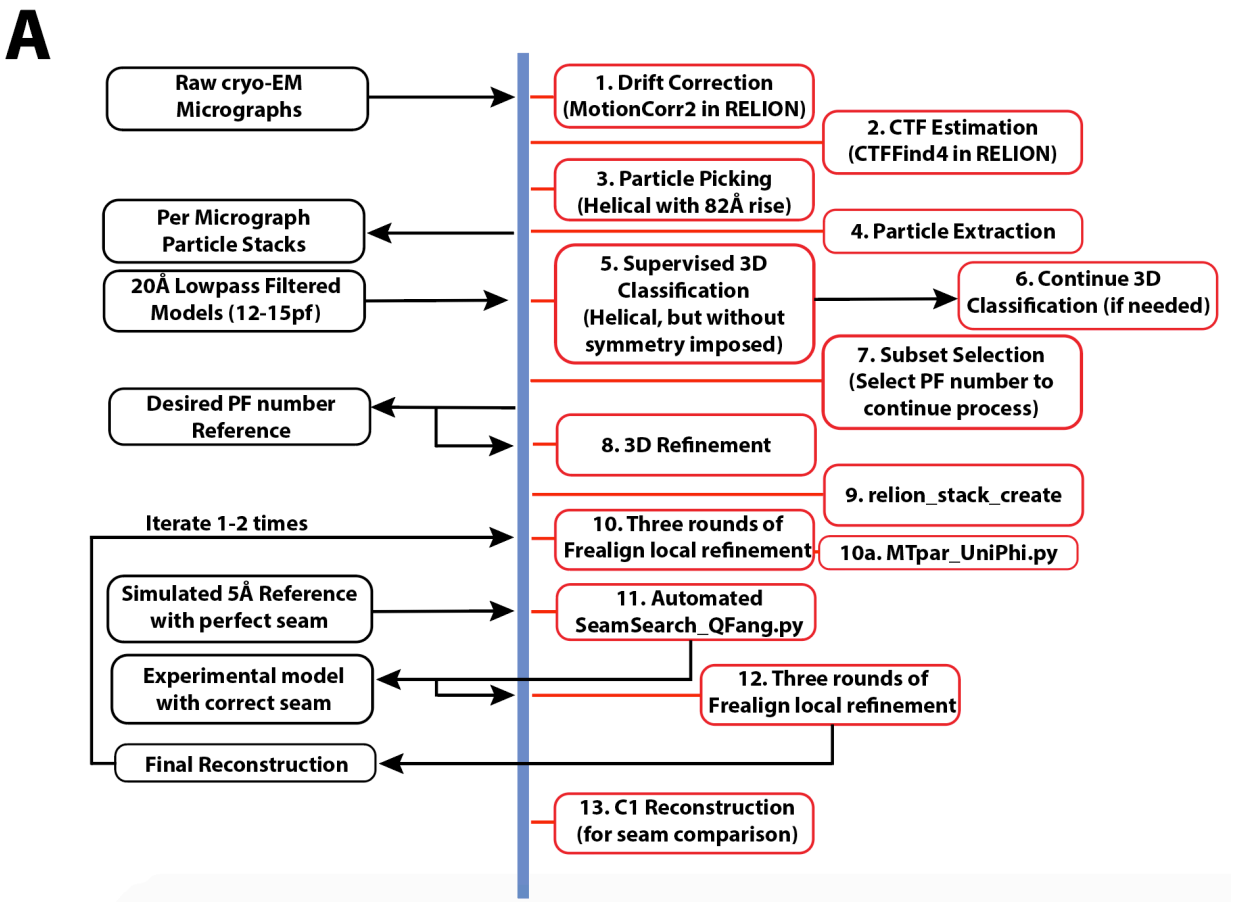

Supplemental Figure 2.2 Data processing pipeline. **(A)** The above pipeline was used for the processing of the MTs within this manuscript. Upon realization that classification by protofilament number was insufficient, the 3D model generated from that (slightly twisted), and a traditional straight model were used to sub-classify all 13pf particles. This yielded a straight 3D class, and an even more twisted class. These two classes were used as references for yet another 3D classification, which yielded the 13pf 4-start structure and the 13pf 3-start structure. Further classification failed to produce any new conformations.

Chapter Three

The encapsulin from *Thermatoga maritima* is a flavoprotein and has a symmetry matched ferritin-like cargo protein

Note: This chapter switches gears from previous chapters and focuses on the structure-function relationships of bacterial organelles known as encapsulins. Although the biological samples are unique and unrelated, the use of cryo-EM and the development of specialized processing techniques are what also facilitated these studies. In particular, the symmetry expansion algorithms were crucial for determining these structures, as well as that of the L-WD40 domain of Kif21B (a kinesin that decorates MTs, as of yet unpublished). This chapter is the culmination of a collaboration with Caleb Cassidy-Amstutz in Dave Savage's lab. The majority of this chapter will focus on the structural characterization and insights gained through the cryo-EM portions of the project, while much of the essential biochemistry was contributed by Caleb. In addition to formalizing this work within this dissertation, Rob Nichols and myself are in the midst of writing up these findings for publication. It should be noted right off the bat that without Rob, Caleb, and Dave, this project would not have been possible. Also, a co-first author paper with Rob characterizing a completely new encapsulin with a novel function is currently on BioRxiv and being revised for eLIFE. Instead of pasting that paper herein, I have focused this chapter on culminating the current data on the original encapsulins characterization to better prepare this story for publication.*

3.1 Abstract

Recently, a new family of protein-based 'organelles' was discovered in bacteria, known as bacterial nanocompartments, or interchangeably, encapsulins. Encapsulins assemble into a virus-like icosahedral particle with a ~25-50nm shell which encapsulates a variety of different cargo proteins. The ability to compartmentalize is crucial, whether to create a unique chemical environment to facilitate a reaction, or to isolate toxic intermediates. With the recent discovery of encapsulins, many fundamental questions remain regarding the assembly principles and biological function. In order to answer a few of these questions, the *T. maritima* encapsulin was biochemically and structurally characterized herein. During purification and analysis, this encapsulin was determined to be a flavoprotein, where the icosahedral shell binds a flavin, FMN, at the interface between subunits. Because this encapsulin uses redox chemistry to reduce soluble iron in the cytosol, we show that encapsulins may not be simply passive barriers, but may play a direct and active role in the function of the encapsulated cargo. Furthermore, we used cryo-EM to show that cargo proteins use a form of symmetry-matching to facilitate encapsulation and stoichiometry. In the case of the *T. maritima* encapsulin, the pentameric cargo protein binds to the pentameric-axis of the icosahedral shell. Taken together, this work is one of the first characterizations of these new encapsulin protein complexes, and it will be exciting to see the field progress as we learn more.

* Robert J. Nichols[1], Benjamin LaFrance[1], Naiya R. Phillips, Luke M. Oltrogge, Luis E.Valentin-Alvarado, Amanda J. Bischoff, Eva Nogales[2], David F. Savage[2]. *Discovery and characterization of a novel family of prokaryotic nanocompartments involved in sulfur metabolism*. **bioRxiv,** 2020.

3.2 Introduction

Over the years, numerous protein-based organelle-like compartments have been discovered in prokaryotes. Historically, bacterial microcompartments such as the carboxysome have dominated the field [113]. Bacterial microcompartments are often formed from hundreds—if not thousands—of copies of subunits. By definition, microcompartments are comprised of multiple different protein subunits that self-assemble into an icosahedral mega-complex ranging from 80-500nm in diameter [114-116].

Relatively recently, a new family of bacterial compartment known as encapsulins was discovered [117]. These encapsulins are more streamlined, often containing a single shell protein and a single cargo protein usually around 25-50nm in diameter [118, 119]. The cargo protein often has enzymatic function, often related to redox chemistry, as is the case for the dye-decolorizing peroxidase (DyP) found in encapsulins from *Brevibacterium linens* and *Rhodococcus jostii* [120, 121].

Another example of the redox role within encapsulins is found in the hyperthermophilic bacteria *Thermatoga maritima*, where the cargo is a ferritin-like protein (FLP). This encapsulin and FLP cargo protein will be the major focus herein. Ferritins are quite common throughout prokaryotes and eukaryotes, and the function of both ferritins and FLPs is to sequester soluble iron, Fe(II), from the intracellular environment, mineralize it into Fe(III), and release Fe(II) again as necessary. The purpose of mineralization is to prevent the soluble iron from spontaneously reacting with reactive oxygen species. Left unchecked, Fe(II) and reactive oxygen species will lead to the Fenton reaction and cause significant DNA damage.

All encapsulins to date have been structural homologs to the HK97 bacteriophage, following the canonical Johnson fold for the capsid protein [119]. Despite the structural homology, the DNA and protein sequences can be extremely divergent. This has hampered the discovery of new encapsulins, as early genetic explorations for new encapsulins have been anchored in previously identified encapsulin genes. In collaboration with Rob Nichols in the Savage Lab, we tackled this hurdle—identifying and characterizing a member of a completely new family of encapsulins. This work was recently published on bioRxiv [122], and is currently under review in eLIFE. However, this chapter will take a step back, instead taking a closer look at the first encapsulin discovered—providing new insights into the role of compartmentalization and FLP function.

The first extensive biochemical characterization of an encapsulin was performed by Sutter *et al* in 2008 [117]. Purified endogenously, x-ray crystallographic experiments resolved the structure of the encapsulin shell protein. Additionally, a short 8 amino-acid targeting sequence of the FLP cargo protein was identified near the 5-fold axis of the encapsulin. Based on homology model and related structures, the FLP cargo was hypothesized to have 5-fold symmetry by Sutter, and later confirmed through structure determination by

a different group [123]. Because the cargo symmetry appeared to match the 5-fold symmetry on the icosahedral shell, it was hypothesized that there may be symmetry matching that occurs between encapsulin shells and their cargo proteins. With this initial baseline of work, we set out to test this symmetry-matching hypothesis by determining structure of the encapsulin shell in complex with the cargo protein. Along the way, we found a few additional surprises that are mentioned below.

3.3 Results and Discussion

3.3.1 The T. maritima encapsulin is a flavoprotein

One of the most fascinating observations was that during the *T. maritima* encapsulin purification, a yellow coloration to the liquid tracked perfectly with the pure encapsulin fractions. Initially we assumed that this yellow tint was due to the presence of encapsulated iron. Interestingly, upon purification of an encapsulin lacking the FLP cargo (incapable of sequestering iron), the yellow color persisted (Figure 3.1 C). Upon determining a high-resolution structure of the encapsulin there was clear density for a flavin mononucleotide (FMN) bound to the shell protein (Figure 3.1 B). Furthermore, it shows a well-defined π-π stacking interaction with a tryptophan residue at position 90 (W90). Given that the encapsulin studied here was purified by heterologous expression, it is conceivable that the FMN molecule is a side-effect of the protocol non-natural host species. However, the fact that the biological implications for this bacterial nanocompartment suggest its involvement in redox chemistry, a flavin molecule facilitating electron transport is not out of the ordinary.

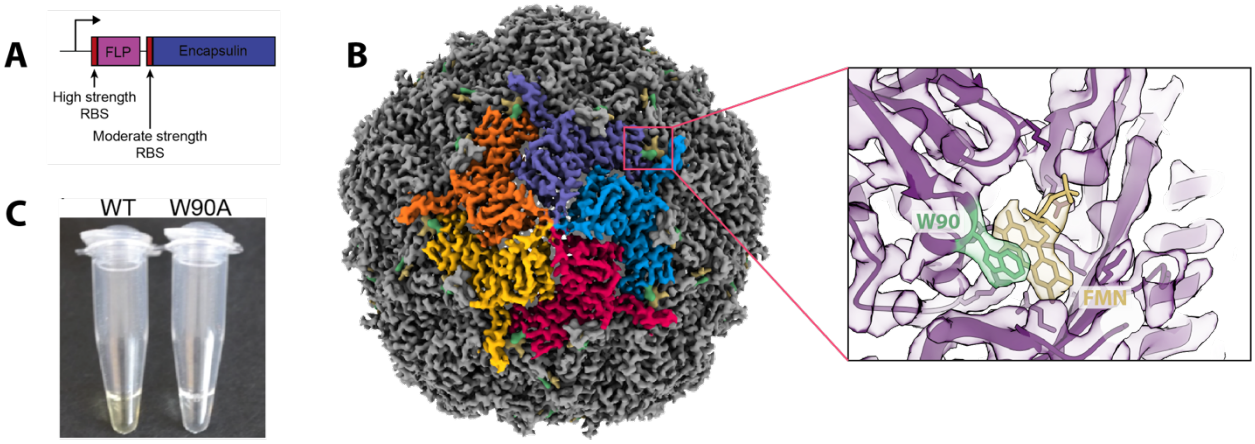

Figure 3.1 Structure determination of the encapsulin shell. **(A)** shows the genetic layout of the encapsulin vector used to maximize the number of FLP-cargo proteins per encapsulin. Cryo-EM analysis showing the clear flavin density in **(B)**. The photo in **(C)** shows the yellow coloration (left aliquot) apparent in all fractions that contained encapsulin throughout the purification.

Upon reflection, the yellow coloration is typical for flavoproteins. In order to biochemically confirm that the *T. maritima* encapsulin shell contained FMN, the absorbance spectrum of the purified encapsulin was compared to riboflavin and pure FMN alone. All three shared a similar trend in their spectral profiles (Figure 3.2 A). Additionally, the presence of FMN was confirmed by mass spectrometry (data from Caleb not shown).

Taken together, all these data strongly support the idea that the encapsulin studied here is a previously undiscovered flavoprotein. Interestingly, the early work described in Sutter's dissertation identifies a yellow coloration to the crystals when determining the initial structure (Figure 3.2 B). Originally, I assumed that this coloration was due to the birefringence commonly observed in protein crystals. However, the recent evidence discussed above suggests that the coloration is the result of FMN bound to the shell. Upon careful examination of the electron density of the 2008 *T. maritima* encapsulin crystal structure, there appears to be extra density around the W90 residue. This weak density could easily be explained from a lower occupancy of the FMN in the endogenous sample originally used, or from variations in rotomer conformations for the W90.

3.3.2 The Tryptophan at position 90 is necessary for FMN binding, despite poor conservation among all encapsulins

Upon determining the 3.3Å cryo-EM structure for the encapsulin and observing the interactions between the FMN and W90, I wanted to probe the effect a tryptophan-to-alanine mutation (W90A), and whether or not this aromatic deletion would perturb FMN binding. After purification of the W90A mutation it was clear that no yellow coloration was observed in the sample (Figure 3.1 C), nor was there any FMN density observed in the cryo-EM structure for the W90A mutant encapsulin.

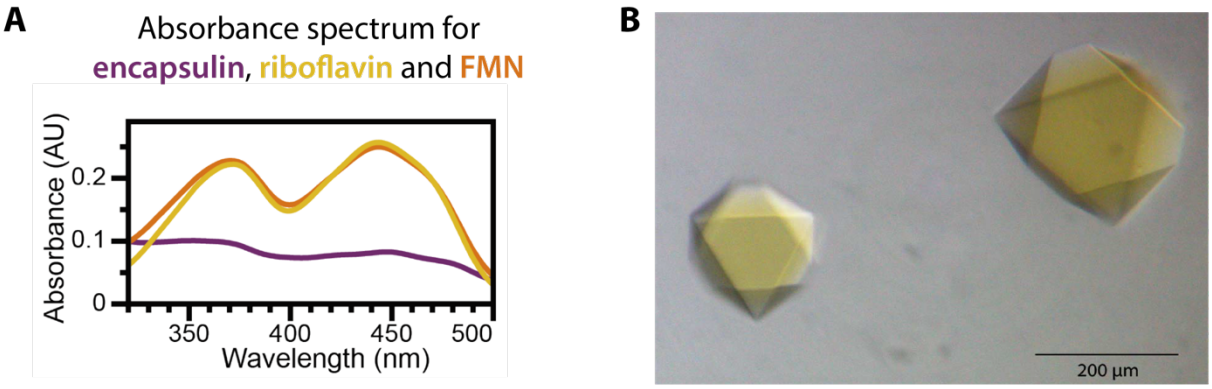

Figure 3.2: Spectroscopic analysis shows the encapsulin appears to bind a flavin molecule. Absorbance spectrum for encapsulin (purple), riboflavin (yellow), and FMN (orange). Although the encapsulin has a significantly reduced concentration, the maximum and minimum values line up well with those observed for riboflavin and FMN **(A)**; courtesy of Caleb Cassidy-Amstutz. Taken from the Sutter's dissertation, panel **(B)** shows the crystal morphologies used for crystallographic data collection with a yellow hue [124].

Given the fact that all previous studies on encapsulins have not identified a flavin bound to the shell, I wanted to see how many of the known encapsulin genes contained the W90 residue critical for FMN binding. Multiple sequence alignment revealed that all encapsulin structures determined from other organisms do not share this critical tryptophan. In fact, a majority of all known encapsulins do not contain a tryptophan at this position, and only about 20% of annotated encapsulin genes contained this tryptophan. Interestingly, all encapsulins that contain W90 tryptophan also have FLP as their cargo protein. Perhaps, the presence of the W90 may serve as a proxy for FMN binding and help inform targeted

studies within the diverse of encapsulin field. These results point to the idea that the flavin may play some role in the biological function of these compartments.

To my knowledge, the presence of a flavin bound to an encapsulin shell indicates the first time that a bacterial nanocompartment has been directly implicated in the reaction of its cargo protein, besides playing the more passive structural role as a diffusion barrier/compartment.

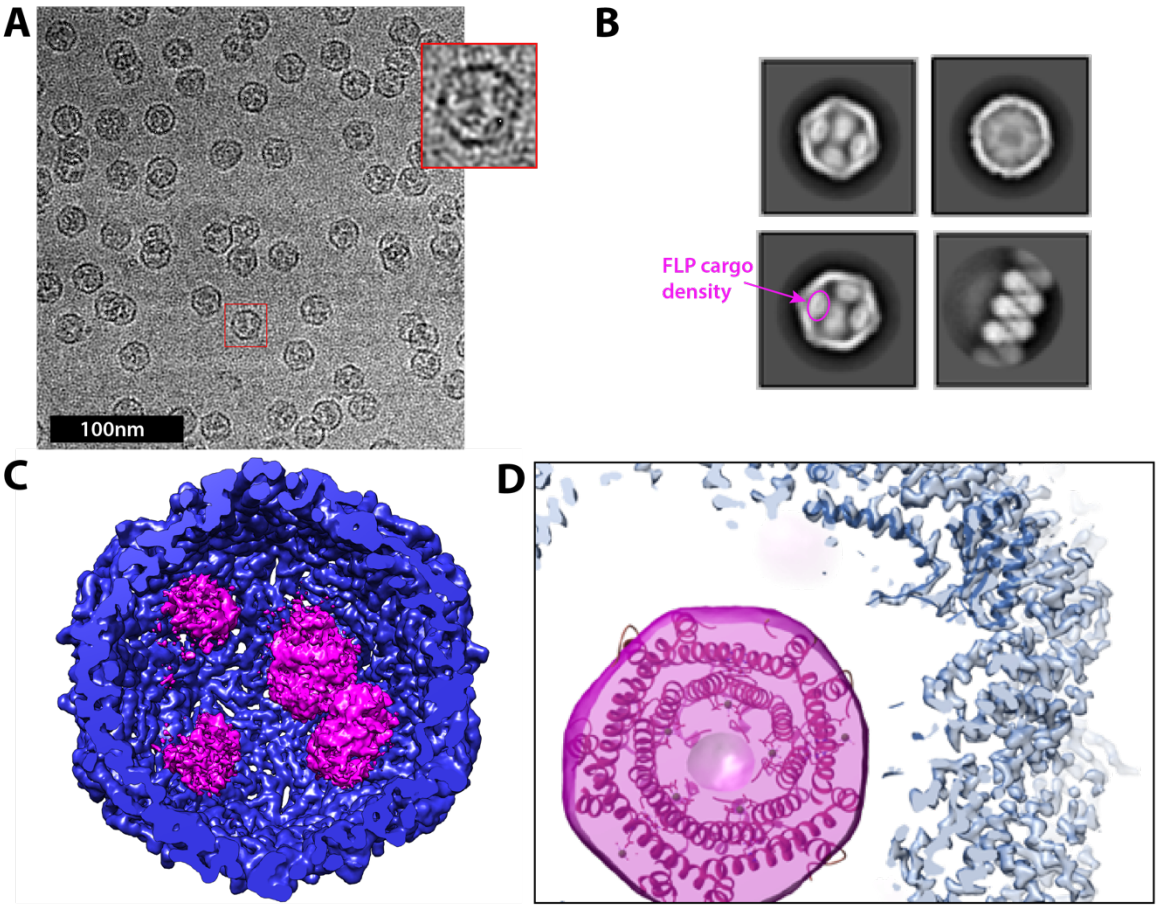

Figure 3.3 Initial processing of the encapsulin reveals density for the FLP-cargo protein. **(A)** shows a raw micrograph collected. The inlay shows an expanded view of a single particle to show that multiple FLP cargo proteins are clearly visible within the encapsulin, even in raw micrographs. Curated 2D class averages in **(B)** further shows FLP density in the 2D class averages, as a well as a small population lacking any cargo protein in the top-right class. The structure in **(C)** is a slice through of the encapsulin in blue showing the weak FLP density in pink. Upon signal subtraction and refinement, the FLP signal is improved in **(D)**, but the orientation of the FLP relative to the shell is ambiguous.

3.3.3 The FLP cargo protein is flexibly bound within the encapsulin shell

However interesting this flavin finding may be, the original goal of this research was to address the hypothesis that encapsulin cargo proteins bind to the shell in a symmetry-matching style. In order to obtain a high-resolution structure of the encapsulin shell, icosahedral symmetry was imposed during the reconstruction. If the FLP cargo bound to the shell in sub-stochiometric amounts, or the binding was not perfectly symmetric within the entire encapsulin shell, then the cargo density would be lost during data processing. Unfortunately, I found this to be the case and the symmetrized map revealed no additional

density for the cargo protein. In order to better visualize the cargo, an asymmetric C1 reconstruction was performed. The C1 structure revealed some cargo density, but there was significant noise due to heterogeneity within the shell (Figure 3.3 C). For example, some of the cargo density was significantly weaker than other cargo density in the reconstruction (compare the lower left pink blob with either of the right blobs). This is evidence for either sub-stochiometric incorporation of cargo (i.e. some particles have 3 FLPs/shell while others may have up to 5 FLPs/shell), or flexibility (i.e. each cargo FLP is not in the same exact location relative to the shell or the neighboring FLP). Although poorly defined, just being able to visualize the cargo was reassuring—especially because there was clear cargo density visible in both the raw micrographs (Figure 3.3 A) and 2D class averages (Figure 3.3 B).

In an attempt to improve the cargo density, signal subtraction was performed to remove signal from the encapsulin shell. The idea behind this effort stems from the fact that the strong shell signal is driving most of the alignment during the reconstruction. Therefore, removing this signal would allow the FLP cargo to carry more weight in each particle image. Signal subtraction allowed for an improvement in the cargo protein (Figure 3.3 D). However, the structure was still not at high enough resolution to identify the orientation or specific location of the cargo protein relative to the shell.

3.3.4 Symmetry expansion and focused classification allow for the FLP location to be unambiguously defined

In order to resolve the structural heterogeneity of the FLP cargo within the encapsulin shell and better identify the interactions governing the encapsulin+FLP assembly, I applied a focused 3D classification strategy based on symmetry expansion which is theorized in Figure 3.4. Symmetry expansion allows for significantly more particles to be used, since the technique multiplies the number of particles by the number of FLPs inside. This approach is theoretically identical to the approach used to better resolve the L-WD40 domain of the kinesin, Kif21B, on microtubules, which is not included in this dissertation but under preparation. The only difference being the transformation matrices used due to different symmetry between samples.

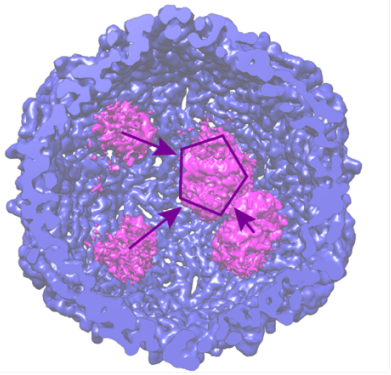

Figure 3.4 Cartoon representation for symmetry expansion and focused classification approach. Arrows denote the symmetry expansion used to place all FLPs into one position, and the pentagon shows the location used for focused classification.

Here the icosahedral symmetry of the encapsulin was used to place all the FLPs into the same exact location in 3D space (arrows in Figure 3.4), followed by a classification of that single location. This strategy enabled us to successfully resolve the FLP to significantly higher resolution (Figure 3.5A). Although the FLP cargo resolution is not high enough to build an atomic model, there are enough features to rigid body dock a crystal structure solved prior to this study (Figure 3.5 B,D)[123].

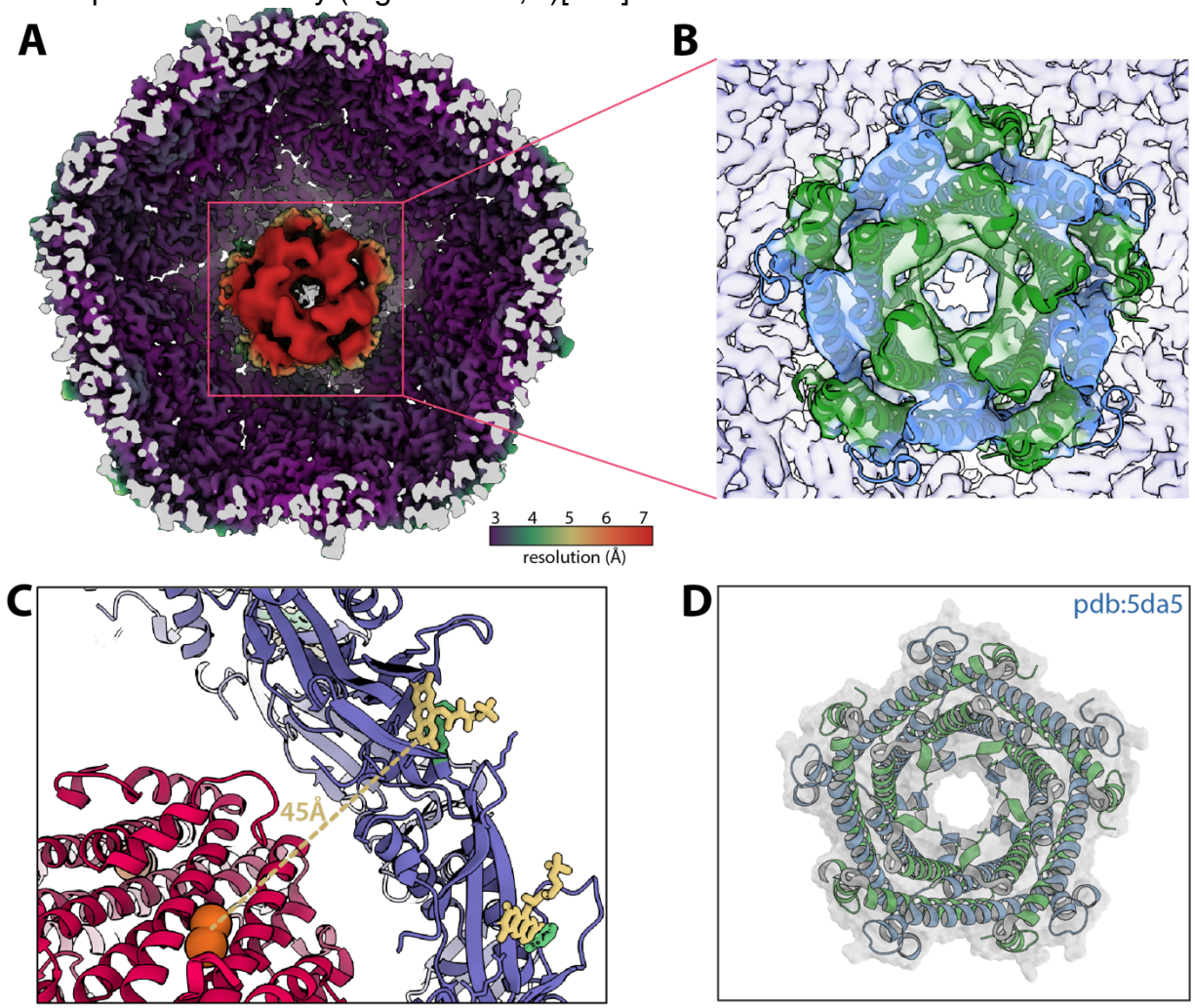

Figure 3.5 Panel **(A)** shows the cryo-EM map resulting from symmetry expansion and focused classification. Colored by local resolution shows that the shell remains at around 3.5Å, whereas the FLP cargo is closer to 7Å. Although only at 7Å, the density is still featureful enough to unambiguously dock the known FLP pentamer structure in **(B)**, with a reference structure provided in **(D)**. The distance between the FLP active site and the FMN molecule bound to the shell is shown in **(C)**. The coloration in **(C)** is as follows: FLP in red with the active site in orange, and the shell in purple, with the bound FMN in yellow interacting with the W90 residue in green.

Upon resolving the FLP density, it is clear that the FLP cargo symmetry does indeed match the symmetry axis of the shell. The FLP, which is a decamer of heterodimers with 5-fold symmetry, is aligned perfectly on the 5-fold axis of the icosahedral. Although this has been intuitively assumed in all previous literature, this offers the first proof of symmetry matching by providing the a well-resolved structure of both the shell and cargo together. With this finding, one could extrapolate that the 3-fold symmetry of the dye-

decolorizing peroxidase (DyP) cargo mentioned briefly in the introduction and found in related encapsulins should bind the 3-fold axis of the shell. Most viruses, encapsulins, and related icosahedral structures often use the 5-fold, 2-fold, or 3-fold axis as a pore to regulate the permeability of the compartmentalized structure, so localizing cargo proteins to these axes and pores may hold some biological significance.

3.3.5 The role of FLP symmetry-matching as well as flavin binding within encapsulins

Encapsulins that package FLP do so in order to regulate iron within the cell. On one hand, encapsulins role is to oxidize soluble ferrous iron and store it within the encapsulin compartment as a mineralized insoluble ferric iron core [117, 123, 125]. The oxidation of iron requires the transfer of an electron from iron to an acceptor. Although this acceptor is often molecular oxygen, a flavin bound to the shell could also serves as an electron acceptor. Unfortunately, when observing iron oxidation under aerobic conditions, there is no significant difference between the flavin-bound encapsulin and the W90A mutant without flavin (Figure 3.6A). Alternatively, the flavin discovered here could serve to help mobilize iron, because the role of these encapsulins is to also release iron when necessary. Under the conditions tested, there was also no clear difference between WT-encapsulin and W90A-encapsulin for iron-release (Figure 3.6B).

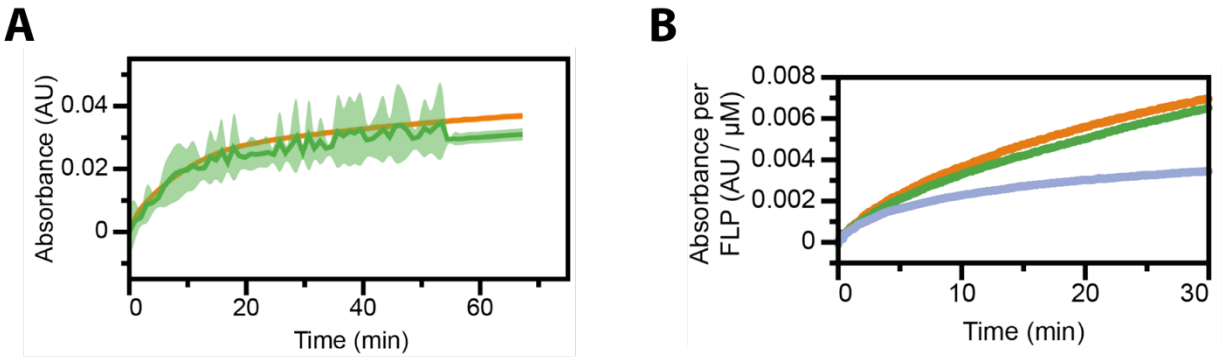

Figure 3.6 Biochemical data regarding the role of flavin in iron mineralization and iron mobilization. **(A)** shows WT (orange) and W90A (green) encapsulins ability to mineralize iron. The difference between the two is not significant. The converse role, the release of iron, is shown in **(B)**, with colors as follows WT (orange), W90A (green), and un-encapsulated FLP (blue); courtesy of Caleb Cassidy-Amstutz.

Another interesting finding spurred by solving the cargo structure was that the active site of the FLP is 45Å away from the shell-bound flavin (Figure 3.5C). The symmetry matching observed between the pentameric FLP and the 5-fold axis of the shell likely keep this distance fairly constrained. Previous experiments regarding electron shuttling have shown shuttling occurs when the donor and acceptor molecules are within 14Å [126]. Given our structure and historical distance data, it is highly unlikely that this flavin is the only acceptor involved in iron mineralization—especially given that the shuttling distance is more than three times greater than previously observed. One possibility is that there is a shuttling molecule between the active site and the shell-bound flavin, as has been shown for other ferritin-like systems [127].

Although the current biochemical evidence suggests there is no clear advantage to containing a flavin, absence of evidence is not evidence of absence. The fact that there is a flavin bound to the shell is a smoking gun, especially given the importance of redox chemistry in the system. From an evolutionary perspective, the flavin could be a vestigial appendage from a time when the flavin was necessary, although this interpretation is highly hand-wavy. Another aspect of this system to consider is that this encapsulin system originates from the bacteria *Thermatoga maritima*, which is an anaerobic fermentative chemoorganotrophic organism. The aerobic conditions used for the iron mineralization assays may allow much higher molecular oxygen as the acceptor molecule than the encapsulin system would experience naturally. Under anaerobic conditions, which are much trickier to replicate in a lab setting, the FMN may serve a more pivotal role. As such, more nuanced are necessary before any claims are made.

Interestingly, release of flavins, and particularly FMN, into the extracellular environment has been shown to confer an important fitness advantage among numerous bacteria [128, 129]. Having an increased local concentration of FMN at a crucial redox hub like the FLP-containing encapsulin logically might have significant advantages that must be addressed in future experiments.

3.4 Conclusions

In this study, we have determined the first structure of an FLP-loaded encapsulin complex in which the cargo protein is clearly resolved. The high-resolution structure of the shell revealed that the *T. maritima* encapsulin is a flavoprotein, as suspected during the purification, and confirmed biochemically. Furthermore, upon learning the significance of a solvent-exposed tryptophan, W90, genetic analysis suggests that numerous other encapsulin flavoproteins may exist which will be an exciting avenue for future studies. Iron regulation is a crucial component of all cells, with catastrophic consequences upon mis-regulation. This study has aided in our understanding of the organization and function of one family of bacterial nanocompartments, known as encapsulins. Better understanding of ferritins, and ferritin-like proteins like the one studied here, provides a fundamental insight into how cells thrive in challenging environments.

3.5 Materials and Methods

In order to determine the structure of the *T. maritima* encapsulin shell:FLP complex, both the shell and cargo were cloned into an pET14 vector, where they were subsequently transformed and expressed in *E. coli* and subsequently purified. Cryo-EM was used for structure determination, after which analysis yielded many of the results discussed here. I have included all protocols here for completeness, but I would like to reiterate the molecular biology and biochemistry was expertly performed by Caleb.

3.5.1 Construction of the T. maritima shell and cargo plasmid

The construct for the *T. maritima* encapsulin shell and FLP-cargo genes was cloned as described previously [130] with a few exceptions. The encapsulin shell gene was ordered and codon optimized for *E. coli* from Genewiz and included a His_6-tag. The FLP-cargo

gene was ordered from IDT as a gBlock that was codon optimized for *E. coli* expression. First, the shell gene was cloned into a pET14 vector followed by the FLP-cargo gene upstream with a higher affinity ribosome binding site (Figure 3.1 A). The rationale for the higher RBS was to maximize the amount of cargo that was expressed and subsequently encapsulated within the shell. For the introduction of the W90A mutation within the shell, golden-gate cloning was performed to introduce the site-specific mutation. All constructs were transformed into DH5α cells for plasmid amplification and sequence verification.

3.5.2 Protein purification of the shell and cargo holo-complex

For expression and purification, the pET14 vector containing the encapsulin shell and FLP-cargo genes where transformed into BL21(DE3) cells and grown in Terrific Broth media at 37°C. Once the cells grew to and OD_{600nm}=0.3, the cells were cooled to 18°C and induced with 500μM IPTG and grown for ~16hrs. Cells were harvested by centrifugation at 4,000rpm at 4°C for 20min and frozen at -20°C until purified.

Cell pellets were thawed to room temperature and resuspended in 50mM Tris-HCl, pH 7.4, 150mM NaCl, and 5mM BME. 10U DNase, 100ug RNase, and 2mg lysozyme were added to the cells and incubated at room temperature for 15min. Cells were further lysed by sonication and cell debris was pelleted at 22,500g for 20min. The supernatant was then heat shocked at 80°C for 3 hours to precipitate most proteins. Because the shell and cargo proteins are from a hyperthermophile, they remain unphased compared to the mesophilic *E.* coli proteins throughout this treatment. The aggregated proteins were pelleted at 25,000g for 25min. The supernatant was then incubated with Nickel-NTA beads for 1hr at 4°C, and washed with 20 column volumes of 20mM $NaPO_4$ pH 7.5, 50mM NaCl, and 30mM Imidazole. Encapsulins were eluted from the Nickel-NTA beads with 3 column volumes of 20mM $NaPO_4$ pH 7.5, 50mM NaCl, and 350mM Imidazole. The elution was concentrated and 500uL was loaded on a Superose 6 10/300 GL column. Fractions were confirmed to contain purified protein for both the encapsulin shell and cargo protein by SDS-PAGE encapsulin. Peak fractions were pooled and concentrated to >20uM. Concentrated encapsulin sample was supplemented with 10% glycerol, aliquoted and flash frozen in liquid nitrogen, and then stored at -80°C until needed.

3.5.3 Cryo-EM sample preparation and data collection

Samples were prepared on Protochips CFlat 1.2/1.3-T grids. Grids were glow discharged on a Tergeo Plasma cleaner prior to use. A frozen aliquot of the *T. maritima* encapsulin was diluted to 2mg/mL in the same buffer as used for size exclusion (20mM $NaPO_4$ pH 7.5, 50mM NaCl) in order to remove the 10% glycerol cryoprotectant used during freezing the aliquots. The 2mg/mL sample was supplemented with 0.05% NP-40 to aid in ice uniformity throughout the cryo-EM grid. 4uL of sample was applied to the grids, and immediately plunge-frozen in liquid ethane using a Vitrobot Mark IV (blot force 10, 2 sec blot, 100% humidity 4°C). The grid was then loaded into a Gatan 626 side entry holder and inserted into a low-base Titan microscope operating at 300 keV. 1,265 micrographs were collected in counting mode at a pixel size of 0.82Å and a total electron exposure of $60e^-$.

3.5.4 Data processing and refinement

Data was processed within the RELION/3.1 pipeline [109]. Individual frames were aligned with MotionCorr2 [69], and with defocus estimation was performed using CTFFIND4 [110]. 1,000 particles were manually picked and 2D classification was performed to generate templates for auto-picking within RELION. Initially 86,124 particles were extracted. Two rounds of 2D classification was performed, followed by a round of 3D classification resulting in 38,952 particles in the final reconstruction which was performed with I1 symmetry. The reconstruction was subjected to multiple iterations of CTF refinement and Bayesian polishing within RELION, ultimately yielding a high-resolution structure for the shell [131]. The atomic model was seeded with the previously determined shell structure (pdb:3dkt), and phenix.real_space_refine function was used to refine the coordinates of 1 subunit surrounded by its nearest neighbors and with FMN bound [111]. Unfortunately, the symmetrization averaged out the substochiometric cargo density and therefore didn't allow for visualization of the FLP. Therefore, a C1 reconstruction was performed, which allowed for modest density of the FLP. Signal subtraction and re-refinement mildly improved the FLP cargo density, but not enough to unambiguously dock the FLP. In order to better resolve the cargo density, symmetry expansion and focused classification was performed. The result yielded a much-improved structure of the FLP cargo protein, which allowed for rigid-body docking of a known FLP crystal structure, pdb:5da5 [123].

3.6 Acknowledgements

We would like to thank to Patricia Grob for EM support, and to Tom Houweling and Abhiram Chintangal for computer support. We are also thankful to Robert Glaeser for the use of the Low-Base Titan microscope. B.L. is supported by NSF-GRFP (1106400). E.N. is a Howard Hughes Medical Institute investigator.

Supplemental Table 3.1: Data collection, 3D reconstruction, and refinement statistics.

Dataset	**Encapsulin Alone**	**Encapsulin with FLP**
Microscope	Low-base Titan	Low-base Titan
Stage Type	Side-entry, Gatan 626	Side-entry, Gatan 626
Voltage (kV)	300	300
Detector	Gatan K2	Gatan K2
Data Collection Software	Leginon	Leginon
Acquisition mode	Counting	Super-Resolution
Physical pixel size (Å)	1.33	0.41
Defocus range (μm)	0.5-2.5	0.5-2.5
Electron exposure (e^-/A^2)	50	50
Reconstruction	**EMD-XXXX**	**EMD-XXXX**
Session	16Aug14	17Mar02
Software	RELION 2.0	RELION 3.1
Particles picked	33,575	86,124
Particles final	19,365	38,952
Extraction box size (pixels)	288^3	512^3
Final pixel size (Å)	1.33	0.82
Map resolution (Sym; Å)	3.9	3.3
Map sharpening B-factor ($Å^2$)	-180	-150
Coordinate refinement		
Software	PHENIX	PHENIX
Refinement algorithm	REAL SPACE	REAL SPACE
Resolution cutoff (Å)	3.9	3.3
$FSC_{model\text{-}vs\text{-}map}$=0.5 (Å)	4.1	3.4
Model		**PDB-XXXX**
Number of residues		264
B-factor overall		38
R.m.s. deviations		
Bond lengths (Å)		0.004
Bond angles (°)		0.625
Validation		
Molprobity clashscore		9.68
Rotamer outliers (%)		0.0
C_β deviations (%)		0.0
Ramachandran plot		
Favored (%)		96.95
Allowed (%)		3.05
Outliers (%)		0.0

Appendix

A.1 Common Microtubule Methods Used in the Nogales Lab

A.1.1 Preparing Tubulin Aliquots

For a majority of microtubule work in the Nogales Lab such as those outlined in Chapter One, we have historically worked with porcine tubulin. Luckily, porcine tubulin is available commercially through Cytoskeleton, Inc (cat #T240-B). To prepare dynamic tubulin aliquots for experimentation, the following procedure is used. Note all buffers and steps should be performed on ice or at 4°C to prevent tubulin from polymerizing.

1. Make 100uL of polymerization (80mM PIPES pH 6.8, 1mM EGTA, 1mM $MgCl_2$, 1mM GTP, 1mM DTT, 10% Glycerol)
2. Add polymerization buffer to resuspend the lyophilized 1mg aliquot of porcine tubulin, carefully pipetting up and down with a pipette to reduce the introduction of air bubbles.
3. Remove the resuspended tubulin and clarify by ultracentrifugation using a TLA-100 rotor operating at 45,000x g for 15min at 4°C. In order to minimize disruption of the pellet, it is best to use a sharpie to label the pellet side of the centrifuge tube, and carefully remove the supernatant from the opposite side.
4. Remove the supernatant, and aliquot 5uL into 0.5mL Eppendorf tubes on ice.
5. Flash freeze in liquid nitrogen and store at -80°C until ready to use.

These aliquots will be at 100uM. Using convention in the field, this corresponds to 10mg/mL, and an A_{280}=10.

Note that porcine tubulin will only polymerize into microtubules at concentrations above 20uM.

If you need to check the concentration of MTs, centrifuge the sample at 16,000g for 20min to pellet the MTs. Remove the supernatant resuspend in 5uL of polymerization buffer. Then dilute the MT sample 10-fold in cold 100mM $CaCl_2$ and leave on ice for 10min to depolymerize MTs before estimating concentration using the proper 1:10 $CaCl_2$ blanking solution as well.

A.1.2 Preparation of Dynamic Microtubules

For dynamic microtubules, simply warm up a water bath to 37°C. Thaw an aliquot of tubulin as prepared above on ice for 10min, then incubate the tubulin at 37°C for 30-60min. Longer than 1 hour, and the tubulin can utilize all of the GTP in the sample and become incompetent. Note that dynamic MTs are highly susceptible to depolymerization and should always be kept at 37°C. This makes them difficult to observe by negative stain, as many of the uranium staining salts can precipitate at 37°C. As such, ideal negative stain samples should be stabilized.

A.1.3 Preparation of Peluroside-stabilized Microtubules

Prepare dynamic MTs as described above, however, prior to polymerization add 1uL of 2mM peluroside to the tubulin aliquot. Peluroside-stabilized MTs are stable for at least 48hrs at both room temperature and 37°C.

A.1.4 Preparation of GMPCPP Microtubules

1. In order to make GMPCPP MTs, first prepare dynamic MTs (45min polymerization at 37°C).
2. Centrifuge the sample at 16,000g for 20min at anywhere from 20-37°C.
3. Remove the supernatant, and resuspend the pelleted microtubules in 5uL Resuspension Buffer.

EM Buffer	250uL 5x BRB80, 2uL 0.5M $MgCl_2$, 1uL 1M DTT, 5uL 10% NP-40, 743uL ddH_2O
Resuspension Buffer	26uL EM Buffer, 4uL 10mM GMPCPP

4. Allow GMPCPP/GTP nucleotides to exchange on ice for 20min.
5. Re-polymerize MTs for 30-60min at 37°C.

Upon re-polymerization, the GMPCPP content should be ~70%, while leftover GTP while remain in 30% of the sample. In most cases, 70% is enough to confer an expanded GTP-like lattice, and stabilize the MT structure. However, if higher purity GMPCPP is desired, the nucleotide exchange and re-polymerization process can be repeated three times to obtain ~90% GMPCPP purity. Longer nucleotide exchanges are insufficient to improve this ratio, and commercial GMPCPP is only available at 10mM concentration thus limiting a more efficient exchange.

A.1.5 Notes on making microtubule grids for cryo-EM

Most cryo-EM grids used for MT samples in the Nogales lab have been Protochips C-Flat 400 mesh 1.2/1.3-T. 400 mesh denotes the size of the squares within the grid (400 squares per inch). Although 200 mesh allows for more real-estate for data acquisition, they are more fragile and prone to cracking while clipping for autoloading. 300 mesh are a great intermediate, allowing more area for imaging, while maintaining some structural integrity during the grid making and loading process. 1.2/1.3 denotes the hole size and space (1.2um diameter holes, spaced 1.2um apart). For MT samples, this ratio works well, because the support structure is critical for allowing adsorption of the MT, while also allowing sufficient hole size to acquire enough images in a dataset. More recently, I have used Quantifoil 0.6/1 UltrAuFoil grids successfully for significantly faster acquisition with beam-shift compensation. However, the traditional C-flat 1.2/1.3 grids also work for beam-shift acquisition, at a reduced collection speed.

If collecting data for beam-shift data collection, the MT concentration must be optimized for uniformity (roughly 1-4 MTs per hole), since medium magnification montages and accurate targeting is not used to specifically image regions with MTs (as is used for traditional targeted imaging). Note that Quantifoil grids must also be treated with 2 drops of chloroform prior to glow discharge in order to remove the formvar layer.

Once a grid type is chosen, grids are glow discharged using a plasma cleaner. For MT samples, the ideal concentration tends to be ~6uM MTs. To make grids, 2-4uL of MTs are applied to the grid and incubated for 30seconds to allow sample adsorption. For the Vitrobot Mark IV optimized settings are 37°C, 100% humidity, blot force 15, 4 second

blot, 1 second drain time. If lower temperatures are desired due to instability of MT-associated proteins (MAPs), peluroside-stabilized MTs can withstand 4°C for a few minutes during the grid preparation process. Also, if decorating with a MAP the same protocol above is followed but with the additional steps.

1. After the first 30sec adsorption of MTs alone, add 4uL of 20uM MAP to the grid
2. Incubate for 30sec.
3. Repeat with a second application of 4uL of 20uM MAP to improve occupancy of MAP bound to the MT.
4. Incubate for 30sec.
5. Prior to blotting, remove 4-5uL of solution on the grid (leaving a small 2-3uL meniscus on the grid). This ensures proper wicking and better control of ice thickness.

Note, all MAPs should also be in a MT compatible buffer such as the EM buffer or Resuspension buffer as listed above. However, stabilized MTs can withstand slight variations in salt and other conditions.

A.1.6 Performing a Microtubule Pelleting Assay

The MT pelleting assay, also known as a co-sedimentation assay is an excellent biochemical method to test whether or not a MAP binds to MTs under certain conditions. The fundamental principle behind this technique relies on the high molecular weight of MTs. Centrifugation will pellet MTs, and if a MAP is in complex with the MT, it will co-sediment into the pellet with the MT. On the other hand, if a MAP does not bind MTs it will be present in the supernatant fraction. The protocol for performing a pelleting assay is outlined below:

1. Pre-warm the TLA-100 rotor, and ultracentrifuge to 37°C.
2. Prepare glycerol cushion (40% glycerol, 1X BRB80, 1mM DTT, and at least 100uM of your stabilizing agent [taxol, GMPCPP, peluroside] or 2mM GTP). You will need at least 20uL per reaction.
3. Prepare the MT+MAP reaction. A few aspects to consider: MT and MAP should be in exactly the same buffer as one another. Always do an MT-alone and MAP-alone control for every experiment. MT concentration should be at least 10uM, and if possible, the MAP should by in ~5-fold excess, or at least stochiometric. Reaction volume should be 20uL, and be incubated for 15-20min at 22-37°C (depending on MAP/MT stability). An example spreadsheet is included at the end of this protocol (Figure A.1).
4. Add 20uL of the glycerol cushion to an ultracentrifuge tube (Beckman 24775 polycarbonate tubes for the TLA-100 rotor). Mark the tube with a sharpie to denote the location of the pellet, to aid in supernatant remove after spinning (pellet will be invisible).
5. Once MT+MAP reaction has proceeded for 20min, carefully add 20uL of the reaction to the top of the glycerol cushion.
6. Ultracentrifuge for 15min at 22-37°C (depending on sample) at 90,000g.
7. Immediately and carefully remove the top 20μL as the supernatant fraction.

8. Carefully remove the remaining liquid to preserve the invisible pellet and discard liquid.
9. Resuspend the pellet in 20μL fresh MT buffer. This will be loaded on an SDS-PAGE as the pellet fraction.
10. Add 6uL of 4x SDS loading dye to both supernatant and pellet fractions.
11. Load 15uL onto a 4-12% NuPAGE Bis-Tris gel and run at 200V for 45min.

Protein Concentration Determination

epsilon (M-1 cm-1)	Protein	A280	[uM]
115000	taxol MT	1.1	9.56
97770	Dam1	2.2	22.50
87760	AR-fl	0.75	8.54

MT Buffer:
20μL 5x BRB80
1μL 100mM DTT
1μL 50mM $MgCl_2$
1μL 2mM taxol
77μL ddH_2O

Pelleting Assay Sample Amounts (uL)

	Reaction	taxol MT	GMPCPP MTs	Dam1	AR-fl	MT Buffer
1	taxol MT only	2.5	0	0	0	17.5
2	taxol MT only	2.5	0	0	0	17.5
3	Dam1 only	0	0	3.75	0	16.25
4	AR-fl only	0	0	0	10	10
5	AR-fl only	0	0	0	10	10
6	taxol MT + Dam1	2.5	0	3.75	0	13.75
7	taxol MT + AR-fl	2.5	0	0	10	7.5

Figure A.1 Example Pelleting Assay Amounts. A sample spreadsheet showing working concentrations and ratios of MTs and MAPs (AR-fl and Dam1, being the MAPs of interest, and the MTs being taxol stabilized).

A.1.7 Subtilisin Cleavage Assay

First, prepare stabilized MTs, as outlined previously. To gently proteolyze the MTs (i.e. remove the flexible C-terminal tails, and the internal K40 loop of α-tubulin, subtilisin is used.

1. Incubate ~2mg/mL of preformed stabilized MTs with 0.05mg/mL subtilisin at 37°C for 20 minutes.
2. Halt the reaction by adding PMSF to 2mM final concentration.
3. Pellet subtilisin cleaved MTs by centrifugation at 16000g for 20min at 37°C.
4. Resuspend pellet in Resuspension buffer (see A.1.4)

This assay, combined with a pelleting assay, is particularly powerful for identifying whether or not a MAP binds to the negatively charged, disordered, 'E-hooks' at the C-termini of both alpha- and beta-tubulin. If binding is specific to these regions, a high-resolution structure will likely be extremely difficult to obtain. Unfortunately, many MAPs rely heavily on these charged electrostatic interactions and occlude structural studies. This can be seen for the CLASP protein later on in the appendix.

A.2 Notes on Advances in Microtubule Processing

Microtubule processing has made leaps and bounds in recent years, which has provided fundamental insights into how MTs function. A few papers in the last few years are excellent examples of this progression, providing two distinct pipelines for high-resolution structure determination [1, 99, 106]. In order to facilitate the structure determinations shown in Chapter Two, I adopted a hybrid processing approach that considers aspects of both the traditional SeamSearch style pipeline of the Nogales Lab with the MIRP pipeline utilized by the Moores Lab. Because the SeamSearch pipeline utilizes numerous customized scripts with old software within many dependencies, it is significantly more difficult to maintain as the field progresses. Despite these issues, the SeamSearch pipeline remains the only available method for structure determination of undecorated MTs. The MIRP pipeline offers a streamlined process within RELION that is significantly more user friendly. As such, I have fused the user-friendly aspects of MIRP, with the powerful processing abilities of the SeamSearch pipeline (Figure A.2B) and provide a brief walk-through of this protocol below.

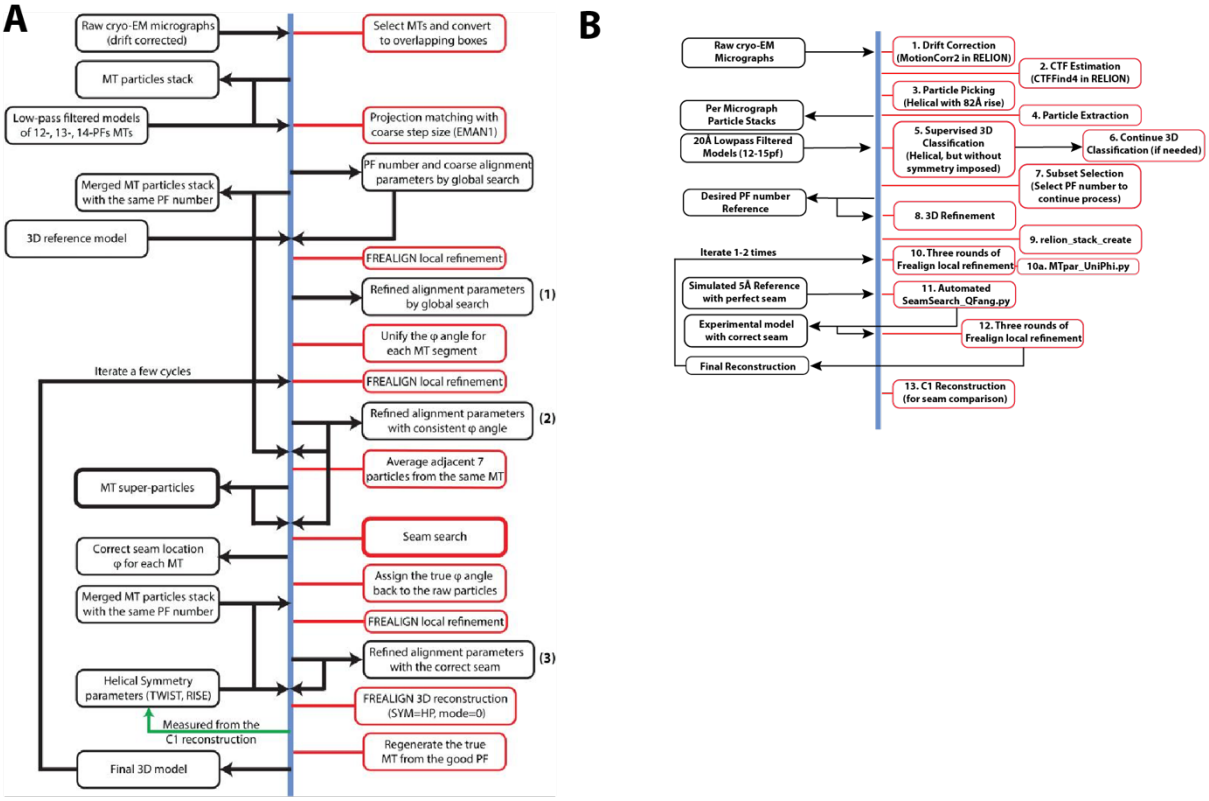

Figure A.2 Examples of Microtubule Processing Pipelines**. (A)** Is the original pipeline that enabled high-resolution structure determination for undecorated MTs [1]. **(B)** The modified pipeline used for Chapter Two, and recommended for future MT studies. Theoretically, this pipeline is nearly equivalent to the original, except for recommendations in newer and more sophisticated programs and built-in automations as outlined in the above text.

Upon data collection on the microscope, import the raw frames into the RELION framework. Use MotionCorr2 within RELION to perform drift correction on the raw data. The advent of Bayesian Polishing and CtfRefine has reduced the need of the patch-based

alignments (i.e. 5x5, 5x7, etc. patches), especially given the strong per-particle signal for MTs. After drift-correction, continue with CTFFind4 (also within RELION).

Manually picking within RELION is still recommended for undecorated MTs, where SeamSearch is still necessary. Relion offers an excellent user interface to pick along helices, which maintains information regarding which particles come from which specific microtubule (a crucial distinction necessary for SeamSearch). Although manual picking is time consuming, I have yet to find an adequate automatic particle picking software that accurately assigns the particles to a single MT (SPRING, crYOLO, TOPAZ, and RELION tried to date). However, if time is of the essence, SPRING and RELION auto-picking appeared to be most successful.

Once all the particles are picked within a dataset, create a stack of the particles within RELION. Binning by 2 or 4 still maintains sufficient information for initial classification. Afterword, perform a supervised 3D classification to assign the protofilament (pf) number to each MT in the dataset (where you provide references for 11-16pf MTs), as outlined by the MIRP pipeline. For porcine MTs, providing only 13pf and 14pf references is often sufficient (for speedier processing), as these datasets often contain only those protofilament numbers. Yeast MTs on the other hand, often have a larger percentage of 12pf MTs, so take care when truncating the number of protofilament references to account for previously observed differences.

After initial classification, there may be a small variation in pf assignment (ie 85% of particles in a given MT are assigned 13pf, interspersed with some single 14pf assignments). There are two schools of thought to address these discrepancies. One method is to assume the entire MT is actually 13pf, and you can reassign the small subset of 14pf particles to the majority 13pf class (3Dclass_force_protofilament.py). The other method is to discard those 14pf outliers, assuming that the inability to classify means those particles won't contribute meaningful signal to the dataset. Given the paucity of pf switching within a single MT in the field of view of an electron microscope, both of these methods are valid, and probably not overlooking any meaningful data regarding pf switching.

Upon sorting out all the particles within a given pf class, I recommend performing an initial refinement, then re-extracting and re-centering the particles. Next, use the relion_stack_create function to create a stack for SeamSearch processing. This step is necessary because relion creates particle stacks on a per micrograph basis, whereas the SeamSearch protocol only uses one large stack for the entire dataset. For SeamSearch, the parameter file will also need to be converted to frealign format (convert_relion2fre.py) to account for the different euler angle conventions. This is where the protocol deviates from the MIRP pipeline, in order to accommodate SeamSearch protocols. After conversion to Frealign format, run 3 rounds of Frealign refinement, while normalizing the phi angle between each round (MTpar_UniPhi.py).

In order to successfully determine the seam location for undecorated MTs, a high-resolution reference model must be used for SeamSearch (<5Å). Often times, it is best to create a simulated reference from atomic coordinates with a perfect seam. Over the past year, Qianglin Fang, a post-doc in the Nogales Lab, and myself, have cleaned up the SeamSearch protocol and compiled the numerous independent scripts into a single command (MT_seamsearch_autorun.py). This wraps up all of the processing in section 2 of Figure A.2A, into one package that outputs an optimized parameters file with a more reliable seam location. This parameter file can then be used to reconstruct a final structure. If the final structure has adequate separation of alpha/beta tubulin and a well-defined seam, then the processing done. However, if there is still mixing of the tubulin, these parameters should be feed into additional rounds of frealign and SeamSearch (1-2 iterations) to improve the map quality. All of the scripts for this process can be found at the shared /home/Nogales-share/ repository, or by contacting the author of this dissertation directly.

References

1. Zhang, R. and E. Nogales, *A new protocol to accurately determine microtubule lattice seam location.* J Struct Biol, 2015. **192**(2): p. 245-54.
2. Unger, E., K.J. Bohm, and W. Vater, *Structural Diversity and Dynamics of Microtubules and Polymorphic Tubulin Assemblies.* Electron Microscopy Reviews, 1990. **3**(2): p. 355-395.
3. McIntosh, J.R., et al., *Lattice structure of cytoplasmic microtubules in a cultured Mammalian cell.* J Mol Biol, 2009. **394**(2): p. 177-82.
4. Chaaban, S. and G.J. Brouhard, *A microtubule bestiary: structural diversity in tubulin polymers.* Mol Biol Cell, 2017. **28**(22): p. 2924-2931.
5. Zheng, Y., et al., *Nucleation of microtubule assembly by a gamma-tubulin-containing ring complex.* Nature, 1995. **378**(6557): p. 578-83.
6. Moritz, M., et al., *Microtubule nucleation by gamma-tubulin-containing rings in the centrosome.* Nature, 1995. **378**(6557): p. 638-40.
7. Kollman, J.M., et al., *Microtubule nucleation by gamma-tubulin complexes.* Nat Rev Mol Cell Biol, 2011. **12**(11): p. 709-21.
8. Moores, C.A., et al., *Mechanism of microtubule stabilization by doublecortin.* Mol Cell, 2004. **14**(6): p. 833-9.
9. des Georges, A., et al., *Mal3, the Schizosaccharomyces pombe homolog of EB1, changes the microtubule lattice.* Nat Struct Mol Biol, 2008. **15**(10): p. 1102-8.
10. Vitre, B., et al., *EB1 regulates microtubule dynamics and tubulin sheet closure in vitro.* Nat Cell Biol, 2008. **10**(4): p. 415-21.
11. Maurer, S.P., et al., *EBs recognize a nucleotide-dependent structural cap at growing microtubule ends.* Cell, 2012. **149**(2): p. 371-82.
12. Howes, S.C., et al., *Structural differences between yeast and mammalian microtubules revealed by cryo-EM.* J Cell Biol, 2017. **216**(9): p. 2669-2677.
13. Howes, S.C., et al., *Structural and functional differences between porcine brain and budding yeast microtubules.* Cell Cycle, 2017: p. 1-22.
14. Mandelkow, E.M., et al., *On the surface lattice of microtubules: helix starts, protofilament number, seam, and handedness.* J Cell Biol, 1986. **102**(3): p. 1067-73.
15. Chretien, D. and R.H. Wade, *New data on the microtubule surface lattice.* Biol Cell, 1991. **71**(1-2): p. 161-74.
16. Kikkawa, M., et al., *Direct visualization of the microtubule lattice seam both in vitro and in vivo.* J Cell Biol, 1994. **127**(6 Pt 2): p. 1965-71.
17. Sosa, H. and R.A. Milligan, *Three-dimensional structure of ncd-decorated microtubules obtained by a back-projection method.* J Mol Biol, 1996. **260**(5): p. 743-55.
18. Sandblad, L., et al., *The Schizosaccharomyces pombe EB1 homolog Mal3p binds and stabilizes the microtubule lattice seam.* Cell, 2006. **127**(7): p. 1415-24.
19. Deng, X., et al., *Four-stranded mini microtubules formed by Prosthecobacter BtubAB show dynamic instability.* Proc Natl Acad Sci U S A, 2017. **114**(29): p. E5950-E5958.
20. Wang, F., et al., *A structural model of flagellar filament switching across multiple bacterial species.* Nat Commun, 2017. **8**(1): p. 960.
21. Nogales, E., S.G. Wolf, and K.H. Downing, *Structure of the alpha beta tubulin dimer by electron crystallography.* Nature, 1998. **391**(6663): p. 199-203.
22. Lowe, J., et al., *Refined structure of alpha beta-tubulin at 3.5 A resolution.* J Mol Biol, 2001. **313**(5): p. 1045-57.

23. Menendez, M., et al., *Control of the structural stability of the tubulin dimer by one high affinity bound magnesium ion at nucleotide N-site.* J Biol Chem, 1998. **273**(1): p. 167-76.
24. Nogales, E., et al., *High-resolution model of the microtubule.* Cell, 1999. **96**(1): p. 79-88.
25. Mitchison, T. and M. Kirschner, *Dynamic instability of microtubule growth.* Nature, 1984. **312**(5991): p. 237-42.
26. Drechsel, D.N. and M.W. Kirschner, *The minimum GTP cap required to stabilize microtubules.* Curr Biol, 1994. **4**(12): p. 1053-61.
27. Caplow, M. and J. Shanks, *Evidence that a single monolayer tubulin-GTP cap is both necessary and sufficient to stabilize microtubules.* Mol Biol Cell, 1996. **7**(4): p. 663-75.
28. Schiff, P.B., J. Fant, and S.B. Horwitz, *Promotion of microtubule assembly in vitro by taxol.* Nature, 1979. **277**(5698): p. 665-7.
29. Dumontet, C. and M.A. Jordan, *Microtubule-binding agents: a dynamic field of cancer therapeutics.* Nat Rev Drug Discov, 2010. **9**(10): p. 790-803.
30. Ojima, I., et al., *Drug discovery targeting cell division proteins, microtubules and FtsZ.* Bioorg Med Chem, 2014. **22**(18): p. 5060-77.
31. Zhang, R., et al., *Mechanistic Origin of Microtubule Dynamic Instability and Its Modulation by EB Proteins.* Cell, 2015. **162**(4): p. 849-59.
32. Alushin, G.M., et al., *High-resolution microtubule structures reveal the structural transitions in alphabeta-tubulin upon GTP hydrolysis.* Cell, 2014. **157**(5): p. 1117-29.
33. Akhmanova, A. and M.O. Steinmetz, *Tracking the ends: a dynamic protein network controls the fate of microtubule tips.* Nat Rev Mol Cell Biol, 2008. **9**(4): p. 309-22.
34. Honnappa, S., et al., *An EB1-binding motif acts as a microtubule tip localization signal.* Cell, 2009. **138**(2): p. 366-76.
35. Maurer, S.P., et al., *EB1 accelerates two conformational transitions important for microtubule maturation and dynamics.* Curr Biol, 2014. **24**(4): p. 372-84.
36. Maurer, S.P., et al., *GTPgammaS microtubules mimic the growing microtubule end structure recognized by end-binding proteins (EBs).* Proc Natl Acad Sci U S A, 2011. **108**(10): p. 3988-93.
37. Zhang, R., et al., *Structural insight into TPX2-stimulated microtubule assembly.* Elife, 2017. **6**.
38. Brouhard, G.J. and L.M. Rice, *The contribution of alphabeta-tubulin curvature to microtubule dynamics.* J Cell Biol, 2014. **207**(3): p. 323-34.
39. Hamel, E. and C.M. Lin, *Guanosine 5'-O-(3-thiotriphosphate), a potent nucleotide inhibitor of microtubule assembly.* J Biol Chem, 1984. **259**(17): p. 11060-9.
40. Roychowdhury, S. and F. Gaskin, *Magnesium requirements for guanosine 5'-O-(3-thiotriphosphate) induced assembly of microtubule protein and tubulin.* Biochemistry, 1986. **25**(24): p. 7847-53.
41. Hyman, A.A., et al., *Role of GTP hydrolysis in microtubule dynamics: information from a slowly hydrolyzable analogue, GMPCPP.* Mol Biol Cell, 1992. **3**(10): p. 1155-67.
42. Wieczorek, M., et al., *Microtubule-associated proteins control the kinetics of microtubule nucleation.* Nat Cell Biol, 2015. **17**(7): p. 907-16.
43. Roostalu, J., N.I. Cade, and T. Surrey, *Complementary activities of TPX2 and chTOG constitute an efficient importin-regulated microtubule nucleation module.* Nat Cell Biol, 2015. **17**(11): p. 1422-34.
44. Rice, L.M., E.A. Montabana, and D.A. Agard, *The lattice as allosteric effector: structural studies of alphabeta- and gamma-tubulin clarify the role of GTP in microtubule assembly.* Proc Natl Acad Sci U S A, 2008. **105**(14): p. 5378-83.

45. Mandelkow, E.M. and E. Mandelkow, *Unstained microtubules studied by cryo-electron microscopy. Substructure, supertwist and disassembly.* J Mol Biol, 1985. **181**(1): p. 123-35.
46. Chretien, D., et al., *Determination of microtubule polarity by cryo-electron microscopy.* Structure, 1996. **4**(9): p. 1031-40.
47. Mandelkow, E.M., E. Mandelkow, and R.A. Milligan, *Microtubule dynamics and microtubule caps: a time-resolved cryo-electron microscopy study.* J Cell Biol, 1991. **114**(5): p. 977-91.
48. Kellogg, E.H., et al., *Insights into the Distinct Mechanisms of Action of Taxane and Non-Taxane Microtubule Stabilizers from Cryo-EM Structures.* J Mol Biol, 2017. **429**(5): p. 633-646.
49. von Loeffelholz, O., et al., *Nucleotide- and Mal3-dependent changes in fission yeast microtubules suggest a structural plasticity view of dynamics.* Nat Commun, 2017. **8**(1): p. 2110.
50. Kueh, H.Y. and T.J. Mitchison, *Structural plasticity in actin and tubulin polymer dynamics.* Science, 2009. **325**(5943): p. 960-3.
51. Fourniol, F.J., et al., *Template-free 13-protofilament microtubule-MAP assembly visualized at 8 A resolution.* J Cell Biol, 2010. **191**(3): p. 463-70.
52. Redwine, W.B., et al., *Structural basis for microtubule binding and release by dynein.* Science, 2012. **337**(6101): p. 1532-6.
53. Mizuno, N., et al., *Dynein and kinesin share an overlapping microtubule-binding site.* EMBO J, 2004. **23**(13): p. 2459-67.
54. Garnham, C.P., et al., *Multivalent Microtubule Recognition by Tubulin Tyrosine Ligase-like Family Glutamylases.* Cell, 2015. **161**(5): p. 1112-1123.
55. Subramanian, R., et al., *Insights into antiparallel microtubule crosslinking by PRC1, a conserved nonmotor microtubule binding protein.* Cell, 2010. **142**(3): p. 433-43.
56. Kellogg, E.H., et al., *Near-atomic cryo-EM structure of PRC1 bound to the microtubule.* Proc Natl Acad Sci U S A, 2016. **113**(34): p. 9430-9.
57. Liu, T., et al., *Structural Insights of WHAMM's Interaction with Microtubules by Cryo-EM.* J Mol Biol, 2017. **429**(9): p. 1352-1363.
58. Bechstedt, S., K. Lu, and G.J. Brouhard, *Doublecortin recognizes the longitudinal curvature of the microtubule end and lattice.* Curr Biol, 2014. **24**(20): p. 2366-75.
59. Ettinger, A., et al., *Doublecortin Is Excluded from Growing Microtubule Ends and Recognizes the GDP-Microtubule Lattice.* Curr Biol, 2016. **26**(12): p. 1549-55.
60. Mozziconacci, J., et al., *Tubulin dimers oligomerize before their incorporation into microtubules.* PLoS One, 2008. **3**(11): p. e3821.
61. Wang, H.W., et al., *Assembly of GMPCPP-bound tubulin into helical ribbons and tubes and effect of colchicine.* Cell Cycle, 2005. **4**(9): p. 1157-60.
62. Chretien, D., S.D. Fuller, and E. Karsenti, *Structure of growing microtubule ends: two-dimensional sheets close into tubes at variable rates.* J Cell Biol, 1995. **129**(5): p. 1311-28.
63. Wang, H.W. and E. Nogales, *Nucleotide-dependent bending flexibility of tubulin regulates microtubule assembly.* Nature, 2005. **435**(7044): p. 911-5.
64. Guesdon, A., et al., *EB1 interacts with outwardly curved and straight regions of the microtubule lattice.* Nat Cell Biol, 2016. **18**(10): p. 1102-8.
65. Atherton, J., et al., *A structural model for microtubule minus-end recognition and protection by CAMSAP proteins.* Nat Struct Mol Biol, 2017. **24**(11): p. 931-943.
66. Maurer, S.P., et al., *Seeded microtubule growth for cryoelectron microscopy of end-binding proteins.* Methods Mol Biol, 2014. **1136**: p. 247-60.

67. Suloway, C., et al., *Automated molecular microscopy: the new Leginon system.* J Struct Biol, 2005. **151**(1): p. 41-60.
68. Mastronarde, D.N., *Automated electron microscope tomography using robust prediction of specimen movements.* J Struct Biol, 2005. **152**(1): p. 36-51.
69. Zheng, S.Q., et al., *MotionCor2: anisotropic correction of beam-induced motion for improved cryo-electron microscopy.* Nat Methods, 2017. **14**(4): p. 331-332.
70. Zhang, K., *Gctf: Real-time CTF determination and correction.* J Struct Biol, 2016. **193**(1): p. 1-12.
71. Lander, G.C., et al., *Appion: an integrated, database-driven pipeline to facilitate EM image processing.* J Struct Biol, 2009. **166**(1): p. 95-102.
72. Ludtke, S.J., P.R. Baldwin, and W. Chiu, *EMAN: semiautomated software for high-resolution single-particle reconstructions.* J Struct Biol, 1999. **128**(1): p. 82-97.
73. Grigorieff, N., *FREALIGN: high-resolution refinement of single particle structures.* J Struct Biol, 2007. **157**(1): p. 117-25.
74. Kimanius, D., et al., *Accelerated cryo-EM structure determination with parallelisation using GPUs in RELION-2.* Elife, 2016. **5**.
75. Egelman, E.H., *A robust algorithm for the reconstruction of helical filaments using single-particle methods.* Ultramicroscopy, 2000. **85**(4): p. 225-34.
76. Emsley, P., et al., *Features and development of Coot.* Acta Crystallogr D Biol Crystallogr, 2010. **66**(Pt 4): p. 486-501.
77. Brown, A., et al., *Tools for macromolecular model building and refinement into electron cryo-microscopy reconstructions.* Acta Crystallogr D Biol Crystallogr, 2015. **71**(Pt 1): p. 136-53.
78. Nicholls, R.A., F. Long, and G.N. Murshudov, *Low-resolution refinement tools in REFMAC5.* Acta Crystallogr D Biol Crystallogr, 2012. **68**(Pt 4): p. 404-17.
79. Murshudov, G.N., et al., *REFMAC5 for the refinement of macromolecular crystal structures.* Acta Crystallogr D Biol Crystallogr, 2011. **67**(Pt 4): p. 355-67.
80. Brouhard, G.J. and L.M. Rice, *Microtubule dynamics: an interplay of biochemistry and mechanics.* Nat Rev Mol Cell Biol, 2018. **19**(7): p. 451-463.
81. Howard, J. and A.A. Hyman, *Growth, fluctuation and switching at microtubule plus ends.* Nat Rev Mol Cell Biol, 2009. **10**(8): p. 569-74.
82. Tropini, C., et al., *Islands containing slowly hydrolyzable GTP analogs promote microtubule rescues.* PLoS One, 2012. **7**(1): p. e30103.
83. Vemu, A., et al., *Severing enzymes amplify microtubule arrays through lattice GTP-tubulin incorporation.* Science, 2018. **361**(6404).
84. Bieling, P., et al., *CLIP-170 tracks growing microtubule ends by dynamically recognizing composite EB1/tubulin-binding sites.* J Cell Biol, 2008. **183**(7): p. 1223-33.
85. Dixit, R., et al., *Microtubule plus-end tracking by CLIP-170 requires EB1.* Proc Natl Acad Sci U S A, 2009. **106**(2): p. 492-7.
86. Komarova, Y., et al., *Mammalian end binding proteins control persistent microtubule growth.* J Cell Biol, 2009. **184**(5): p. 691-706.
87. Seetapun, D., et al., *Estimating the microtubule GTP cap size in vivo.* Curr Biol, 2012. **22**(18): p. 1681-7.
88. Manka, S.W. and C.A. Moores, *Microtubule structure by cryo-EM: snapshots of dynamic instability.* Essays Biochem, 2018. **62**(6): p. 737-751.
89. Richard McIntosh, J., et al., *Ultrastructural Analysis of Microtubule Ends.* Methods Mol Biol, 2020. **2101**: p. 191-209.

90. Zhang, R., B. LaFrance, and E. Nogales, *Separating the effects of nucleotide and EB binding on microtubule structure.* Proc Natl Acad Sci U S A, 2018. **115**(27): p. E6191-E6200.
91. Estevez-Gallego, J., et al., *Structural model for differential cap maturation at growing microtubule ends.* Elife, 2020. **9**.
92. Nawrotek, A., M. Knossow, and B. Gigant, *The determinants that govern microtubule assembly from the atomic structure of GTP-tubulin.* J Mol Biol, 2011. **412**(1): p. 35-42.
93. Pecqueur, L., et al., *A designed ankyrin repeat protein selected to bind to tubulin caps the microtubule plus end.* Proc Natl Acad Sci U S A, 2012. **109**(30): p. 12011-6.
94. Katsuki, M., D.R. Drummond, and R.A. Cross, *Ectopic A-lattice seams destabilize microtubules.* Nat Commun, 2014. **5**: p. 3094.
95. Tong, D. and G.A. Voth, *Microtubule Simulations Provide Insight into the Molecular Mechanism Underlying Dynamic Instability.* Biophys J, 2020. **118**(12): p. 2938-2951.
96. Roostalu, J., et al., *The speed of GTP hydrolysis determines GTP cap size and controls microtubule stability.* Elife, 2020. **9**.
97. Amos, L. and A. Klug, *Arrangement of subunits in flagellar microtubules.* J Cell Sci, 1974. **14**(3): p. 523-49.
98. Tilney, L.G., et al., *Microtubules: evidence for 13 protofilaments.* J Cell Biol, 1973. **59**(2 Pt 1): p. 267-75.
99. Cook, A.D., et al., *A microtubule RELION-based pipeline for cryo-EM image processing.* J Struct Biol, 2020. **209**(1): p. 107402.
100. Chretien, D. and S.D. Fuller, *Microtubules switch occasionally into unfavorable configurations during elongation.* J Mol Biol, 2000. **298**(4): p. 663-76.
101. Howes, S.C., et al., *Structural differences between yeast and mammalian microtubules revealed by cryo-EM.* The Journal of Cell Biology, 2017. **216**(9): p. 2669-2677.
102. Ma, M., et al., *Structure of the Decorated Ciliary Doublet Microtubule.* Cell, 2019. **179**(4): p. 909-922 e12.
103. von Loeffelholz, O., et al., *Nucleotide– and Mal3-dependent changes in fission yeast microtubules suggest a structural plasticity view of dynamics.* Nature Communications, 2017. **8**(1): p. 2110.
104. Cross, R.A., *Microtubule lattice plasticity.* Curr Opin Cell Biol, 2019. **56**: p. 88-93.
105. Janosi, I.M., D. Chretien, and H. Flyvbjerg, *Structural microtubule cap: stability, catastrophe, rescue, and third state.* Biophys J, 2002. **83**(3): p. 1317-30.
106. Debs, G.E., et al., *Dynamic and asymmetric fluctuations in the microtubule wall captured by high-resolution cryoelectron microscopy.* Proc Natl Acad Sci U S A, 2020.
107. Rice, S., et al., *A structural change in the kinesin motor protein that drives motility.* Nature, 1999. **402**(6763): p. 778-84.
108. Schorb, M., et al., *Software tools for automated transmission electron microscopy.* Nat Methods, 2019. **16**(6): p. 471-477.
109. Zivanov, J., et al., *New tools for automated high-resolution cryo-EM structure determination in RELION-3.* Elife, 2018. **7**.
110. Rohou, A. and N. Grigorieff, *CTFFIND4: Fast and accurate defocus estimation from electron micrographs.* J Struct Biol, 2015. **192**(2): p. 216-21.
111. Adams, P.D., et al., *PHENIX: a comprehensive Python-based system for macromolecular structure solution.* Acta Crystallogr D Biol Crystallogr, 2010. **66**(Pt 2): p. 213-21.
112. Afonine, P.V., et al., *New tools for the analysis and validation of cryo-EM maps and atomic models.* Acta Crystallogr D Struct Biol, 2018. **74**(Pt 9): p. 814-840.

113. Shively, J.M., *Inclusion bodies of prokaryotes.* Annu Rev Microbiol, 1974. **28**(0): p. 167-87.
114. Chowdhury, C., et al., *Diverse bacterial microcompartment organelles.* Microbiol Mol Biol Rev, 2014. **78**(3): p. 438-68.
115. Kerfeld, C.A., S. Heinhorst, and G.C. Cannon, *Bacterial microcompartments.* Annu Rev Microbiol, 2010. **64**: p. 391-408.
116. Yeates, T.O., M.C. Thompson, and T.A. Bobik, *The protein shells of bacterial microcompartment organelles.* Curr Opin Struct Biol, 2011. **21**(2): p. 223-31.
117. Sutter, M., et al., *Structural basis of enzyme encapsulation into a bacterial nanocompartment.* Nat Struct Mol Biol, 2008. **15**(9): p. 939-47.
118. Giessen, T.W., et al., *Large protein organelles form a new iron sequestration system with high storage capacity.* Elife, 2019. **8**.
119. Nichols, R.J., et al., *Encapsulins: molecular biology of the shell.* Crit Rev Biochem Mol Biol, 2017. **52**(5): p. 583-594.
120. Ahmad, M., et al., *Identification of DypB from Rhodococcus jostii RHA1 as a lignin peroxidase.* Biochemistry, 2011. **50**(23): p. 5096-107.
121. Rahmanpour, R. and T.D. Bugg, *Assembly in vitro of Rhodococcus jostii RHA1 encapsulin and peroxidase DypB to form a nanocompartment.* FEBS J, 2013. **280**(9): p. 2097-104.
122. Nichols, R.J., et al., *Discovery and characterization of a novel family of prokaryotic nanocompartments involved in sulfur metabolism.* bioRxiv, 2020: p. 2020.05.24.113720.
123. He, D., et al., *Structural characterization of encapsulated ferritin provides insight into iron storage in bacterial nanocompartments.* Elife, 2016. **5**.
124. Sutter, M., *Structural basis of enzyme encapsulation into a bacterial nanocompartment*. 2008, ETH.
125. McHugh, C.A., et al., *A virus capsid-like nanocompartment that stores iron and protects bacteria from oxidative stress.* EMBO J, 2014. **33**(17): p. 1896-911.
126. Page, C.C., et al., *Natural engineering principles of electron tunnelling in biological oxidation-reduction.* Nature, 1999. **402**(6757): p. 47-52.
127. MacKenzie, E.L., K. Iwasaki, and Y. Tsuji, *Intracellular iron transport and storage: from molecular mechanisms to health implications.* Antioxid Redox Signal, 2008. **10**(6): p. 997-1030.
128. Fuller, S.J., et al., *Extracellular electron transport-mediated Fe(III) reduction by a community of alkaliphilic bacteria that use flavins as electron shuttles.* Appl Environ Microbiol, 2014. **80**(1): p. 128-37.
129. von Canstein, H., et al., *Secretion of flavins by Shewanella species and their role in extracellular electron transfer.* Appl Environ Microbiol, 2008. **74**(3): p. 615-23.
130. Cassidy-Amstutz, C., et al., *Identification of a Minimal Peptide Tag for in Vivo and in Vitro Loading of Encapsulin.* Biochemistry, 2016. **55**(24): p. 3461-3468.
131. Zivanov, J., T. Nakane, and S.H.W. Scheres, *A Bayesian approach to beam-induced motion correction in cryo-EM single-particle analysis.* IUCrJ, 2019. **6**(Pt 1): p. 5-17.